IEEE Access
Multidisciplinary ⋮ Rapid Review ⋮ Open Access Journal

Received 7 August 2023, accepted 28 August 2023, date of publication 18 September 2023, date of current version 28 September 2023.

Digital Object Identifier 10.1109/ACCESS.2023.3316726

RESEARCH ARTICLE

CogniFlow-Drop: Integrated Modular System for Automated Generation of Droplets in Microfluidic Applications

RAUNO JÕEMAA[1,2], NAFISAT GYIMAH[1], KANWAL ASHRAF[1], KAISER PÄRNAMETS[1], (Member, IEEE), ALEXANDER ZAFT[1], OTT SCHELER[2], TOOMAS RANG[1,2], (Senior Member, IEEE), AND TAMÁS PARDY[1,2], (Member, IEEE)

[1]Thomas Johann Seebeck Department of Electronics, Tallinn University of Technology, 19086 Tallinn, Estonia
[2]Department of Chemistry and Biotechnology, Tallinn University of Technology, 19086 Tallinn, Estonia

Corresponding author: Rauno Jõemaa (rauno.joemaa@taltech.ee)

This work was supported in part by the Estonian Science Agency (ETAg) under Grant PRG620 and Grant MOBTP109, in part by the European Union's Horizon 2020 Research and Innovation Program under Grant 668995, in part by the Tallinn University of Technology (TTU) Development Program (2016–2022) under Project 2014−2020.4.01.16.0032, in part by the Estonian Research Council, in part by the European Commission, and in part by the Tallinn University of Technology.

ABSTRACT Droplet microfluidics enables studying large cell populations in chemical isolation, at a single-cell resolution. Applications include studying cellular response to drugs, cell-to-cell interaction studies. Such applications need a reliable and repeatable droplet generation with high monodispersity. Most systems used in research rely on manual tuning of flow parameters on off-the-shelf instruments. Setups are highly customized, limiting reproduction of experimental results. We propose an integrated, modular system for automated aqueous droplet generation with high monodispersity. The system provides dynamic feedback control of droplet size and input pressure. Input pressure is generated by two piezoelectric micropumps. Droplet sizes are determined via light intensity measurement in an LED-photodiode setup. The system is capable of wireless communication and has a low enough power consumption for battery-powered operation. We report on the assembly and the underlying working principle, as well as an in-depth experimental evaluation of the performance of the proof-of-concept prototype in aqueous droplet generation. Evaluation was performed on a modular as well as on a system level. During module-level evaluations, aqueous droplets were generated in a light mineral oil + Span 80 surfactant carrier medium, using 3 different flow-focusing junction geometries. The presented prototype had a significantly faster pressure stabilization time (10 s) compared to a syringe pump-based reference setup (120 s). During system-level evaluation, deionized water droplets were generated in a carrier medium of HFE7500 + PEG-PFPE triblock surfactant. Resultant droplet sizes were benchmarked with microscopy. The system was able to repeatedly generate mono- and polydisperse droplets on demand, with CVs between 5-10% in the ∼50-200 μm droplet diameter range.

INDEX TERMS Lab-on-a-Chip, microfluidic, automation, pulsatile flow, droplet size control, droplet generation rate control, optical feedback, pressure feedback, closed-loop control, wireless communication.

I. INTRODUCTION

Droplet microfluidics enables studying the response of cell populations to specific chemicals, in isolation, at a very high throughput [1]. Chemical isolation is given by encapsulating cells into aqueous droplets in an immiscible carrier medium, together with the chemicals for their treatment. For example, antibiotics and resistant bacteria, to screen for antimicrobial susceptibility, or circulating multi-drug resistant tumor cells and chemotherapy drugs to screen for drug response among other analysis targets [2], [3]. Working in droplets enables 1) higher throughput than conventional batch processing in

The associate editor coordinating the review of this manuscript and approving it for publication was Zhiwu Li.

2) a compact, highly integrated, automatic system as well as 3) continued work with individual droplets downstream [4]. Furthermore, it enables analysis of single-cells, or cell-to-cell interactions [5]. Droplet microfluidics has additional applications in chemical analysis and synthesis, as well as bioanalyses other than cytometry (e.g., nucleic acids) [6].

However, imaging droplet flow cytometry necessitates reliable and repeatable droplet generation with high droplet monodispersity (1-5% [4], [7]) at moderate droplet generation rates (∼1-3 kHz [7]). To date, open-loop control and/or manual tuning of flow parameters to achieve desired droplet sizes and stable droplet generation are most common [8], [9]. However, the target parameters are difficult to achieve and maintain with manual tuning. Thus, automated droplet generation with closed-loop control (or in other words, an inline quality control system of droplet generation) is necessary. Zheng et al. [10] demonstrated a reduction of steady-state error to <2% coefficient of variation (CV) across various flow conditions in droplet digital polymerase chain reaction (PCR) applications [11]. Similarly, Duan et al. [12] achieved high monodispersity (<7.6 CV%) by implementing a closed-loop control strategy, which was at least 90% lower than with open-loop control. Additionally, Zeng and Fu [13] addressed the challenge of predicting droplet size by using closed-loop control to account for the nonlinearity of flow-focusing. Moreover, a novel microfluidic system was developed to optimize cell processing conditions using deep learning algorithms for analyzing sensor data and closed-loop control to update a pressure pump and maintain optimal cell flow speed [14]. Several other works have demonstrated closed-loop control of droplet sizes by tuning flow parameters based on an image/video stream of the flowing droplets [15], [16], [17]. Most demonstrated systems (TABLE 1) used droplet imaging for control. However, overall throughput in camera-based tracking is limited by the imaging throughput of the camera (increasing throughput increases cost and heat dissipation). The price/performance ratio of imaging droplets for flow control (in contrast with cell imaging, which is a different application) is also not optimal.

A compact system with a laser-photodiode setup for bubble tracking was demonstrated in [18]. Such an integrated, compact benchtop setup enables portability between labs, which in turn enables transferring experimental workflows with excellent repeatability. It also allows replication of results, thus enabling virtual parallel labs and digital, rather than physical exchange of results and knowledge. However, at present, widely used setups are an ensemble of off-the-shelf instruments, assembled specifically for the experiment on hand, with little to no integration (TABLE 1). The lack of integration means the setup (and results created with it) cannot be easily transferred between labs. It is also notable that while in microfluidics in general, syringe pumps are the most popular choice due to their flow stability, affordability, and ease of use, in droplet microfluidics, pressure pumps are also very common, as they do not need refilling. The need to refill the syringe causes interruptions in experimental workflows,

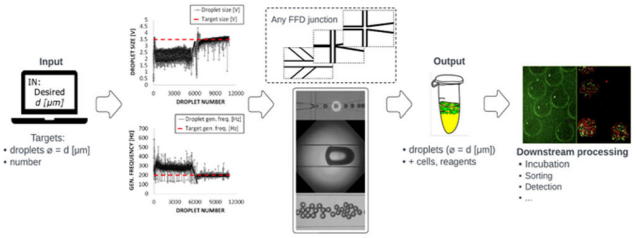

FIGURE 1. CogniFlow-Drop concept: droplets with user-defined process and dimensional parameters are generated automatically from reagents and samples needed by the user, with minimal user interaction, in a compact, standalone device. These can then be collected for further downstream processing, e.g., incubation and detection.

and possibly also the need to recalibrate flow parameters. Finally, in our earlier reviews, we found a pronounced interest towards low-cost instrumentation and the democratization of instruments for droplet microfluidics [4], [19].

As of today, compact, integrated droplet microfluidics instruments, particularly with wireless communication and low-cost hardware, are uncommon. Setups exist that meet some but not all criteria (TABLE 1) for a compact, modular, automated, wirelessly communicating droplet generator.

In this work, we describe a proof-of-concept experimental setup meeting the aforementioned criteria, its underlying methodology, and the evaluation of its performance in droplet generation experiments. The CogniFlow-Drop system concept (Fig. 1) offers the following advantages over the state of the art (TABLE 1):

1. It is integrated and modular (some modules can be swapped out for easy upgrades), improving reliability, and enabling portability. These features ensure that results and workflows are transferable between labs (enabling creation of virtual parallel labs).
2. It is low-cost (∼650€) compared to commonly used experimental setups built from off-the-shelf components. With future development, modularity will enable customization, affordability will open wider collaboration using the platform.
3. Can offer comparable performance to commonly used droplet generation setups through its dual-PID control of droplet size and generation frequency. With future optimizations, can significantly reduce carrier/sample/reagent waste. Furthermore, through automation, can ensure better repeatability without manual recalibration or in-depth knowledge of the technology.
4. Measures droplet generation in real-time via intensity change in a simple LED-photodiode setup (water droplets, passing between, causing a change compared to the carrier medium).
5. Uses tilting mounts to reliably set up chip, light source, and detector alignment, to optimize channel/droplet visibility in a given microfluidic chip. This also increases reproducibility of results.
6. Uses wireless communication, which enables remote control and monitoring of the system.

TABLE 1. Overview of the state-of-the-art feedback-controlled droplet generators compared to our novelty.

Reference	Flow actuation	Flow control algorithm	Continuous phase fluid	Discrete phase fluid	Monodispersity (CV%)	Flow sensor	Integrated & standalone?	Communication
[12]	Programmable pressure pump	PID controller	Silicone oil	Calcium chloride solution	<7.6%	N/A	No	USB
[11]	Pressure pump	PI controller	Silicone oil	Water	2%	Pressure sensor		
[16]	Pressure pump	PID controller	Fluorinated oil	Water	0.32%	N/A		
[13]	Pressure pump	PID controller	Silicone oil	Water	N/A	N/A		
[34]	Microvalves	PI controller	Silicone oil	Water	No steady state errors	N/A		
[35]	Syringe pump, and gas regulator	PI controller	BSA in NaCl	Nitrogen	N/A	N/A		
[36]	Syringe pump	PID controller	Paraffin + 10% Span80	Water	RMSE reduces from 3.4 to 0.48	N/A		
[37]	Pressure pump	Pi controller	Silicone oil	Water	N/A	Pressure sensor		
[18]	Gas-driven	Dual-PID (pressure, bubble size) control	Water + Tween80	C_4F_{10}/CO_2 gas	N/A	Laser-photodiode	**Yes**	
Our work	**Dual piezo pumps**	**Dual -PID (pressure, droplet size/gen. rate) control**	**HFE7500/ mineral oil + tri-block surfactant**	**Water**	**5-10%**	**LED-photodiode**	**Yes**	**WLAN**

7. Has a sufficiently low power consumption (∼8.0 W) that it can be powered from batteries for portable operation (based on the estimated consumption, >4.5h battery life on a 10000 mAh Li-ion power bank).

II. COGNIFLOW-DROP SYSTEM PROTOTYPE

In this section, we present a structural overview of the complete prototype assembly (Section II-A), then in following sections (Section II-B to II-D) overview each system module in detail, including both hardware and software, from a structural as well as functional perspective (working principles).

A. OVERVIEW

The system prototype (Fig. 2/4) was constructed as a compact, modular assembly with an emphasis on ease of use and low hardware cost. In this section, we overview the assembly and subassemblies, and link to sections with further details on each. The system consisted of three main modules (see also block diagram in Fig. 3) and the enclosure:

1) **Electronics module** (Section II-B and Fig. 2/1): functionally responsible for communication, instrument control and signal processing. Physically was constructed as a stack of stages onto which electronic parts were mounted:
   a) *Power supply unit* (PSU) stage (Fig. 2/1/a): mounted the RJ45 adapter, the power switch, the mains connector, and the PSUs (ECS45US05, XP Power).
   b) *Pump controller and pressure sensor stage* (Fig. 2/1/b): mounted the pump controller interface (with the low-level pump controller running on an ESP32 DevKitC board) and pressure regulation board. The stage was shielded from noise from above and below by copper plates attached

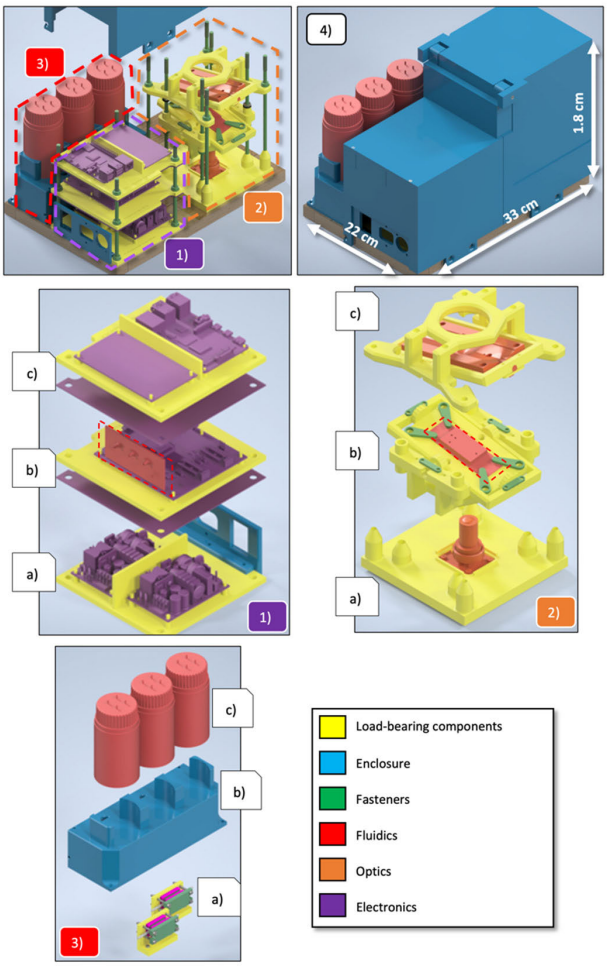

FIGURE 2. Prototype assembly, consisting of modules: (1) electronics module consisting of the power supply stage (a) , the pump driver and pressure sensor stage (b) and the stage that contained the RPi4B as well as the ADC and filtering circuit for the optical sensor (c), plus the corresponding copper shielding plates. (2) The sensorics module, consisting of the base stage with the photodiode and lens (a), the microfluidic chip mount stage (b) and the light source mount stage (c). (3) fluidics module, which included L-mounts for the pumps (a) and a foam-padded enclosure (b), as well as (c) sample, reagent, and product collection containers. (4) The enclosure with 3D printed internal and external walls, as well as a wooden base plate to which all modules were mounted for stability. The M5 bolts mounting the stages of the modules are hidden in the close-up explosion views (1)-(3).

to and grounded through structural conductive threaded rods.

c) *Communication, control, and signal processing stage* (Fig. 2/1/c): mounted the Raspberry Pi 4B (RPI), responsible for system control and communication, and the filter-amplifier, analog-to-digital conversion (ADC) board for the optical sensor.

2) **Sensorics module** (Section II-C and Fig. 2/2): functionally responsible for optical flow rate measurement. Physically also holds the microfluidic droplet generator chip and consists of the following stack of stages:

a) *Photodetector stage* (Fig. 2/2/a): the photodetector PCB and the connecting microscope lens were mounted to the bottom plate.

b) *Chip mount stage* (Fig. 2/2/b): included the chip mount with 3 degrees of freedom (DoF; height, roll, pitch) and a removable microfluidic chip holder.

c) *Light source mount stage* (Fig. 2/2/c): positioned at the top of the sensorics module was an analogous 3 DoF mount stage for the light source as was for the chip mount stage. The light source was an LED, soldered to a 25 mm × 75 mm sized PCB. A diffuser/lens was attached over the LED. Aluminum or large copper area on the PCB was used for heat dissipation from the LED.

3) **Fluidics module** (Section II-D and Fig. 2/3, Fig. 2/1/b, Fig. 2/2/b): functionally responsible for generating droplets from the carrier medium, reagents, and sample(s). Additionally responsible for dampening secondary vibration and sound produced by piezoelectric micropumps.

a) *Pump mount* (Fig. 2/3/a): both pumps were mounted on an L-shaped mount. The pumps were fastened to the mount with shock dampening rubber in between.

b) *Shock- and audibility-dampening piezopump enclosure* (Fig. 2/3/b): 2-part enclosure with rubber padding fitted around the micropumps for additional sound absorption. The top of the enclosure was designed with slots for three 100 ml lab bottles.

c) *Liquid containers* (Fig. 2/3/c): included the reagent and sample containers, as well as the product collector.

d) *Pressure sensors* (mounted to electronics module Fig. 2/1/b)

e) *Fluidic chip* (mounted to sensorics module Fig. 2/2/b)

4) **Enclosure** (Fig. 2/4): held the components together, including the interior walls between compartments, as well as the external enclosure. The base plate was a wooden board of 22 cm × 33 cm × 1.8 cm, selected to provide mechanical support to the assembly. Internal walls were used to route cables and tubing, as well as providing slots for T-junctions that bridged connections between the microfluidic chip, the pumps, and the pressure sensors. All plastic components were 3D printed. Load-bearing components were 3D printed with a Prusa i3 mk3S, the T-junctions [20] with an Anycubic Photon Mono. Electronics and sensorics modules were fastened to the base plate with structural ISO M6 size threaded rods, whose internal components were fastened to load-bearing components with ISO M3 size bolts (metal fasteners are hidden on the explosion views for better clarity). The pump enclosure was fastened to the base plate with ISO M3 size bolts. The chip mount stage was set between spring-loaded knurled nuts (DIN 466 M6) to reduce vibrational sensitivity.

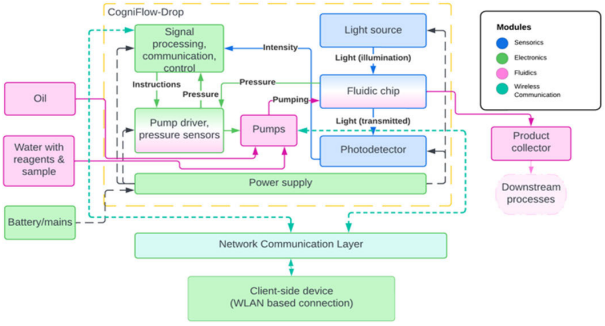

FIGURE 3. CogniFlow-Drop device: in the device, oil-water droplets of a user-defined size are generated, encapsulating cells and reagents of given kinds. The regulation of droplet sizes takes place by means of simultaneous pressure and flow rate control, resulting in a high control precision (in terms of CV% [coefficient of variation] of droplet diameter). The system implements distributed wireless control in an event-triggered manner [25].

B. ELECTRONICS MODULE

1) FLOW CONTROL STRATEGY

For the pressure-driven droplet generator, a dual-PID controller strategy with two feedback loops (inner and outer feedback loops, Fig. 4/a) was designed and implemented:

- The inner feedback loop was used to rapidly reach target pressure levels in the microfluidic chip and to reduce pressure fluctuations, inherently induced by the droplet pinch-off process, the pulsatile nature of the micropumps and the rapid target pressure level approach. The inner loop consisted of PID controllers for each micropump separately.
- The outer feedback loop was used to reach and maintain user defined droplet size and generation rates through discretized light sensor data.

The proposed design of the dual-PID control strategy (depicted on Fig. 4/a) for the CogniFlow-Drop system can be described as follows:

1) The inner PID closed feedback loop used pressure readings from sensors 1 (S_1) and 2 (S_2) of pumps 1 and 2, respectively, as well as pressure readings from sensor 3 (S_3) at the microfluidic chip's output.
2) The PID controller associated with each pump regulated the pressure drop across the chip using the differential pressures (i.e., S_1-S_2, S_1-S_3) as feedback. The accurate and rapid control of pressures produced by the inner feedback loop action improved the stability and precision of the outer feedback loop.
3) The outer PID controller achieved user-defined droplet size and droplet generation frequency set points (d_{set} and f_{set}) by adjusting the pressure of pump 1 and 2 respectively (i.e., disperse and continuous phase flows). The size related pressure target was derived from using the error (e_d) between the set point (d_{set}) and the average measured droplet size (d_m). The generation frequency related pressure target was derived from using the error (e_f) between the set point (f_{set}) and the average measured droplet generation frequency (f_m). By fixing the disperse phase pressure, the control variable relationships between "droplet size" to "disperse phase pressure" could be made as "droplet size" to "continuous phase pressure", depending on the sensitivity of the target parameter to the fluid phase type [21].

In reference to our earlier work, the PID controller parameters (i.e., proportional gain, integral gain, and derivative gain) were derived using a Genetic Algorithm (GA). The dual-PID control strategy, adapting the framework implemented with MATLAB, Simulink in [22], was modified to include droplet generation frequency control for the presented version of the droplet microfluidics system, using Python.

2) PUMP CONTROLLER AND PRESSURE SENSOR STAGE

The pumping system embedded into CogniFlow-Drop was an updated version of the non-automated dual-channel piezoelectric pumping device demonstrated in our earlier work [23], [24]. Relevant notable modifications to our standalone pump PCBs ([24]) are mentioned in the electronic supporting information (ESI) S1.

While the base design with all its features was carried over, standalone operation (wireless communication and battery power) was not. Wireless communication was not necessary as the pump controller exchanged commands and sensor data, as well as received power, over a USB cable connecting the pump controller (ESP32) to the main controller (RPI). Additional updates were required to be made to the pump controller firmware from the earlier work ([24]) with relevant notable ones mentioned in ESI S1.

3) COMMUNICATION, CONTROL, AND SIGNAL PROCESSING STAGE

RPI was selected as the main controller for the system due to its quad-core processor and extensive interfacing options. It ran Ubuntu desktop (ver. 21.10) with its tasks written in Python 3.9 and C++. With four cores, the RPI was able to dedicate one for each independent task:

1) Communication with the user, over local network, using the methodology described in Section II-B-IV.
2) Communication with the pump hardware described in Section II-B-II.
3) Interpretation of data obtained from the optical sensor, expanded upon in Section II-C.
4) Calculation of pumping pressure targets based on both the measured pressure data (obtained from task 2) and the resolved optical data (obtained from task 3), detailed in Section II-B-I.

The interpretation of links between tasks and their interactions with parts of the system, external from the Raspberry Pi, are shown in Fig. 5, and an explanation with more details about the internal mechanism of each task is described in ESI S2.

4) USER INTERFACE

Data and information flow are critical aspects when considering the design of any bioanalytical device. In our

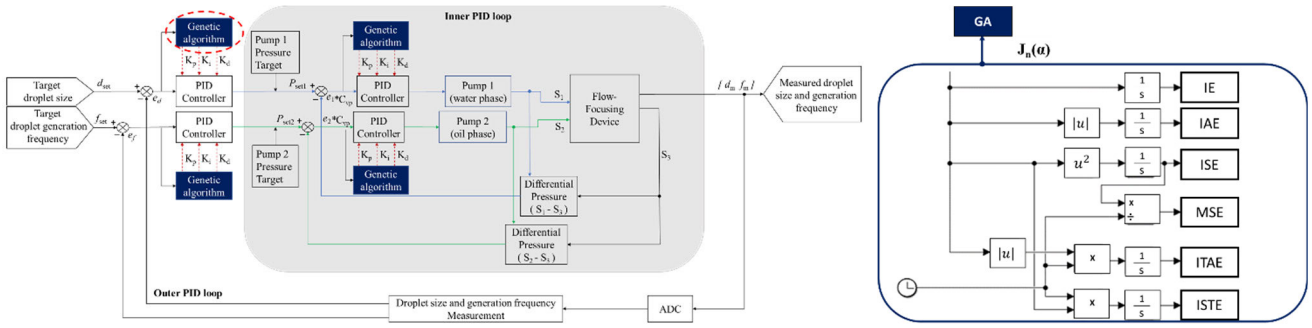

FIGURE 4. a) Structure of dual-loop PID control strategy. The inner feedback loop reduced pressure fluctuations, improved accuracy, and speed of reaching target pressure level. Outer feedback loop adjusted droplet sizes and generation rates based on optical flow rate measurement from module 2 in Fig. 2; b) Structure of PID tuning method with six objective function criteria obtained from using genetic algorithm.

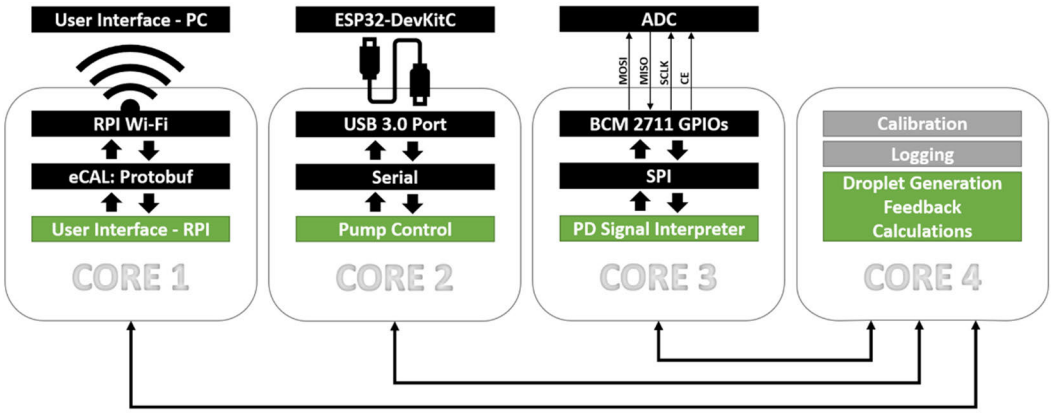

FIGURE 5. Four main tasks (in green) of the system controller were made to run concurrently on separate cores. Core 1 handled user commands received over local network using eCAL API with Protobuf format. Core 2 communicated with the pumping system's control board ESP32-DecKitC via serial protocol. Core 3 received discretized photodiode signal from an ADC in SPI protocol format through Raspberry Pi's BCM 2711 GPIOs and using it to measure running droplet generation parameters. Core 4 managed commands and information from the other three cores to start, stabilize and end droplet generation.

previous work we presented a framework for integrating event-triggered wireless data distribution and information flow into a bioanalytical device [24]. In this work, we focus on structured data serialization (along with metadata) using Google's Protobuf serialization protocol [25]. With this method, the number (and type) of devices in the network could be extended with minor edits to the data structures.

Inter-host communication was performed using an enhanced Communication Abstraction Layer (eCAL, v5.9.5) middleware [27]. The data rate through eCAL was payload dependent, and the employed data-centric communication architecture offered low latency communication with fair reliability.

Data was sent between devices along with a unique device ID and name, chip name, flow rate, transmission/reception status, flag for different process activation, and droplet size (see example in Fig. 6/a) and message ID. On the publisher/sender side, a Protobuf message object (see example in Fig. 6/b), was created based on the data structure defined and serialized using the Protobuf protocol, followed by being broadcast to any listening device. For any device to catch the broadcast data, an eCAL subscriber/receiver function was cyclically polled. Concurrently, the method was used in reverse to transfer data from the controlled device to the controller. Devices could communicate with each other in an event-triggered wireless or wired manner. The overall data transfer mechanism is shown in Fig. 7.

The CogniFlow-Drop prototype could be controlled via the graphical user interface (GUI, Fig. 8) by defining parameters for droplet generation rate and size and passing them on using the available task specific buttons. If the chosen parameters were not within acceptable limits or of the wrong type, an error was presented, asking for appropriate corrections. The entered parameters were serialized by protocol and sent to the other device in the form of messages. Unless manually halted from the GUI, tasks were halted automatically on the controlled device after completion.

5) OPTICAL FEEDBACK SIGNAL ACQUISITION

The digitization PCB before signal processing on RPI, was made with three stages.

```
syntax = "proto3";

package proto_message;

message spec
{
  float dsize       = 1;
  uint32 id         = 2;
  float drate       = 3;
  string status     = 4;
  uint32 command    = 5;
  string deviceName = 6;
  string chipName   = 7;

}
```

(a)

```
# set message content
specific.dsize = dropsize
specific.id = message_id
specific.drate = input_rate
specific.status = status
specific.command = command_nr
specific.deviceName = device_name
specific.chipName = chip_name
print("Status is {}".format(specific.status))
if command_nr != 1:
    print("Droplet size {} and rate {}".format(specific.dsize,specific.drate))
    if chip_name != "None":
        print("Chip under test: {}".format(specific.chipName))
    else:
        print("Chip Name is not defined")

# send message
while ecal_core.ok() and specific.id < repeat_msg:
  if command_nr != 1:
    if inputs_in_range is True:
        pub.send(specific)
        print("Successful tranmission iteration {}".format(specific.id))
```

(b)

FIGURE 6. Communication interface implementation. (a) Data Structure for CogniFlow-Drop: droplet size (dsize), message id, droplet generation rate (drate), sender status/role, operational command, sender device name, and saved calibration parameters named with corresponding microfluidic chip. (b) instances of eCAL-based message transmissions.

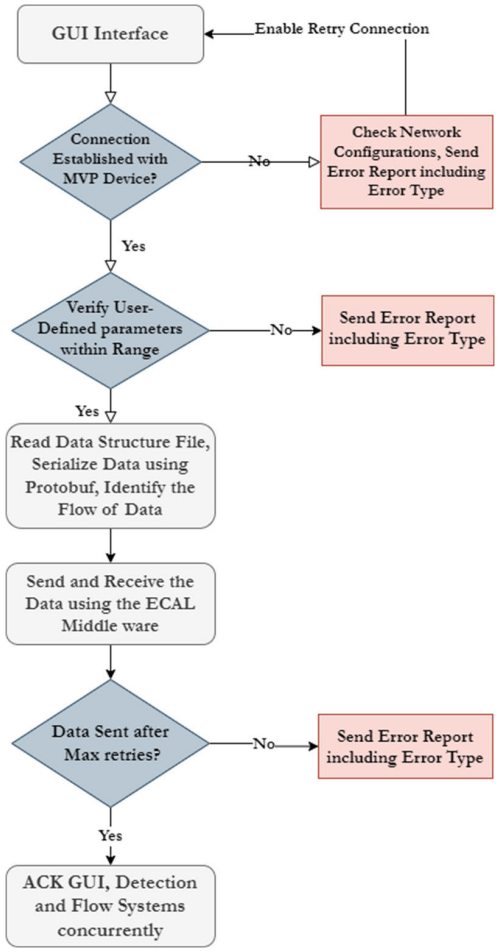

FIGURE 7. Implementation of the communication interface, data transmission, reception, verification, and a Graphical User Interface for accessibility.

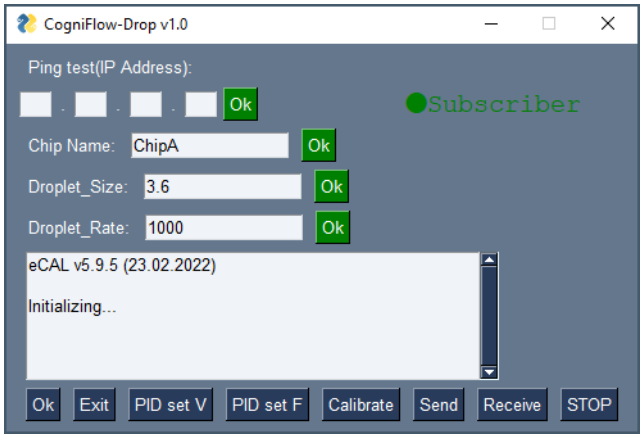

FIGURE 8. ECAL based Graphical User Interface (CogniFlow-Drop v1.0).

The first stage, receiving the feedback signal directly from the sensorics module described in Section II-C, was a 2nd order Sallen-Key low pass filter. The filter was designed for detection of up to 5000 droplets per second without distortions, with a cutoff frequency at ∼7.26 kHz and a quality factor of ∼0.64. Filtering was necessary to reduce noise acquired from the system (in most part from the used switch-mode PSUs).

Before discretization with an ADC, to maximize the information gained from the incoming, filtered optical signal, per bit, an adjustable inverting amplifier stage was used. This enabled scaling of captured waveform to the ADC's analog input limits. Additionally, this filter-amplifier circuit was designed to discard any inherent DC component from the optical signal and bias it instead with 2.5 V, to position it in the middle of the 0 to 5 V ADC measurement window.

The converter used was a 16-bit ADC (ADS8681, Texas Instruments). In the presented version of the system, the PCB on which it was installed was a perforated protoboard, which introduced additional noise to the measured signal due to a non-ideal splitting of digital and analog signals.

C. SENSORICS MODULE

1) DROPLET MEASUREMENT HARDWARE

In our previous works, we demonstrated cost-effective imaging [28] and non-imaging [29] droplet flow sensor

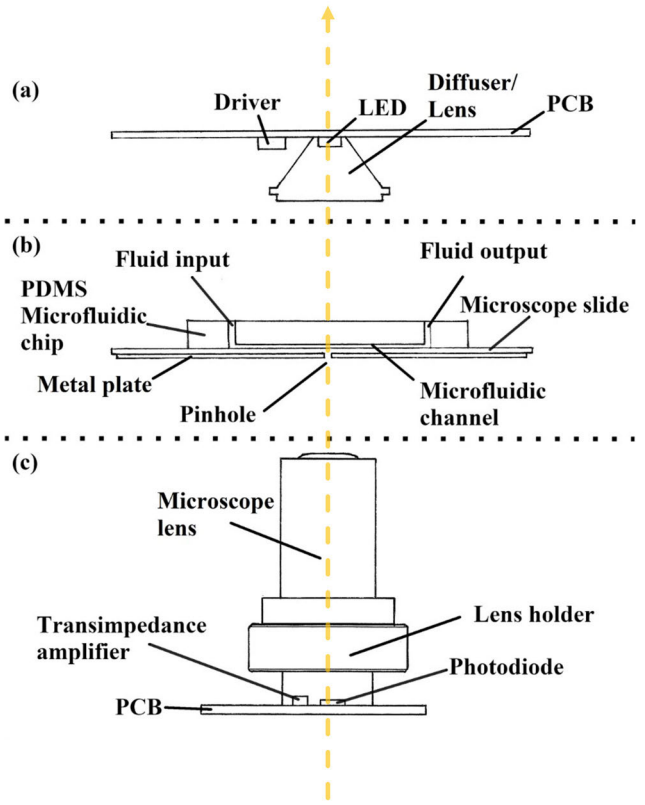

FIGURE 9. Cross-section of the microfluidic droplet measurement system with parts aligned to the axis marked with a dashed yellow line. (a) An LED with an LED driver is soldered to a printed circuit board (PCB) that is used to illuminate the microfluidic chip. In addition, a matted lens is used to diffuse and focus the light. (b) A PDMS-glass microfluidic chip is mounted to the chip holder with a metal plate with a micro-drilled pinhole positioned underneath. (c) A non-imaging photodiode collects light, while a high gain transimpedance amplifier is added nearby. On a custom PCB, components are mounted along with a lens holder and microscope lens.

prototypes with up to 750 frames per second throughput. With cost-effectiveness in mind, a more compact setup with a higher throughput for capturing droplets during generation was constructed as follows (Fig. 9):

- A light source constructed of a cold white 1 W wide-beam LED (Fig. 9/a). Soldered to a PCB with large copper areas for heat dissipation. Current-limited to ∼150 mA using an LED driver.
- The light source was covered with a diffusing lens (Fig. 9/a) to reduce its beam angle and reduce beam intensity variations from smaller misalignments with the sensor axis.
- A PDMS-glass microfluidic chip, further detailed in Section II-D (Fig. 9/b).
- A thin metal plate, with a noise-reducing micro-drilled pinhole (sized proportionally with the chip's junction width), positioned beneath the microfluidic chip to increase the relative dimming impact of a passing droplet (Fig. 9/b).
- Based on Texas instruments application [30], using a 1 MΩ as feedback resistor instead, to obtain a gain of 1 MV/A and a 1.3 pF capacitor for stability at higher frequencies, a photodiode (PD) sensor (Osram SFH 2240, Fig. 9/c) was connected to a transimpedance amplifier (TIA). A 20x microscope lens was mounted to the PCB, over the sensor, for improved focus of the droplets flowing in the microchannel.

Using the droplet flow sensor setup described above, a theoretical detection throughput was raised above 10000 droplets per second.

2) DETECTION OF DROPLET SHADOWS

The chip mount (Section II-A-II-b and Fig. 2/2/b) was positioned between the light sensing PD and the light source, all of which were vertically aligned to the pinhole under the outlet junction of the microfluidic chip (Fig. 9). As generated droplets were moving over the pinhole, a shadow was cast through it, onto the PD. The changing current through the PD was converted to voltage using a high-gain TIA, passed on to a connected filter-amplifier circuit in the electronics module (Section II-B-V and Fig. 2/1). The filtered signal moved through a DC decoupler into an inverting and level-shifting amplifier circuit. The extra amplification also provided compensation when the height of the light source was adjusted. The inversion of the photodiode voltage meant that any increase in the shadow corresponded to an increase in measured voltage. The filtered and amplified photodiode output was discretized with the ADC and sent over to the main control board using SPI. The RPI dedicated 1 of its 4 cores to communicating with the ADC, enabling photodiode voltage sampling rates of up to ∼440 kHz (without an interpretation algorithm).

D. FLUIDICS MODULE

1) DROPLET GENERATION CHIPS

The microfluidic chip designs used in this work were adapted from the group's earlier works, notably the ''Droplet counting chip'' in the ESI of [31]. The principle design (Fig. 10/a) was a flow-focusing device (FFD) laid out on an SU8 mask in multiple copies with different junction widths and geometries. In TABLE 2 the chip designs used in experiments in this work are shown. The mask design is openly available on our GitHub [32]. Silanized silicon-SU8 masks were purchased from the BioMEMS group of the Hungarian Academy of Sciences [33]. PDMS-glass chips were fabricated as follows: 1) PDMS was molded off the mask (PDMS was allowed 3 days at room temperature to cure and degas), 2) the PDMS was punched to create ports using a tissue biopsy tool, 3) PDMS and glass surfaces were cleaned from dust, 4) surfaces were activated with oxygen plasma generated by a handheld corona discharge surface treater, 5) surfaces were bonded, 6) chip walls were coated with Novec™1720 Electronic Grade Coating.

2) MOUNTING OF THE DROPLET GENERATION CHIP

The removable chip holder (Section II-A-II-b) in the sensorics module (Fig. 2/2/b) had a 2 by 2 mm square hole at the

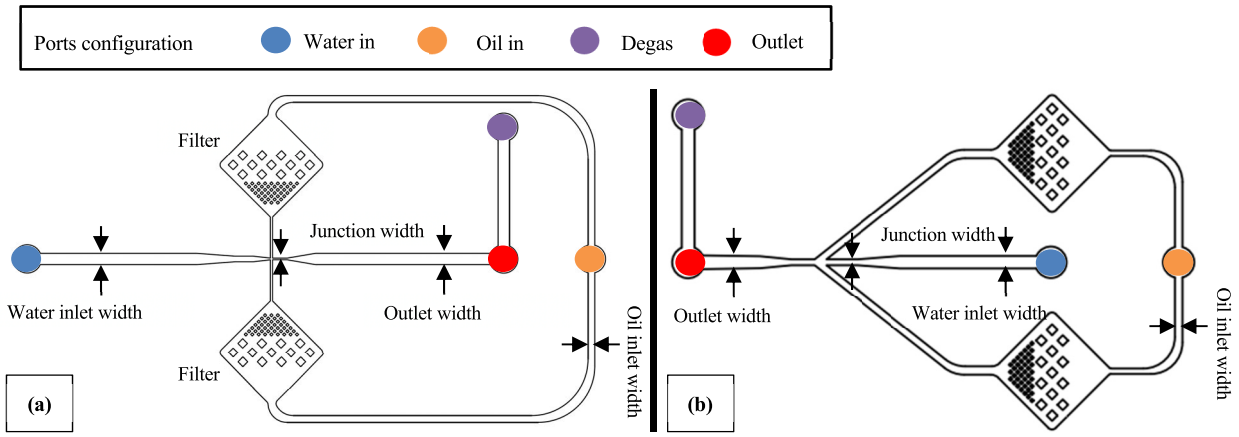

FIGURE 10. Parameterized flow-focusing device for controlled droplet generation. Oil inlet is split equally and filtered through micropillar arrays to prevent impurities on the oil line from clogging the junction. The outlet has a 1 ml gas spring attached to smoothen out flow rate fluctuations coming from the pump. Chip variant A/B (a) had a 90-degree entry in the flow-focusing junction, whereas variant C (b) had a 38.33-degree entry angle and a shorter outlet length. There was no other difference between the 3 chip variants apart from the junction width. Water inlet, outlet and oil line widths were the same.

TABLE 2. Primary/main mould design parameters for microfluidic droplet generator chips.

Chip variant	A	B	C
Junction width [mm]	90	125	280
Junction angle of entry [°]	90	38.33	
Oil inlet width [mm]	360		
Water inlet width [mm]	6		
Outlet width [mm]	0.6		
Number of filters	2		

center, over which the metal plate (Fig. 9/b) with a pinhole was placed. The pinhole was manually centrally aligned with the square hole in the chip holder. Lastly, a droplet generation chip was positioned on the pinhole plate and fastened to the holder. The chip was aligned to have the pinhole beneath the chip's outlet channel, ∼300 μm after the cross-junction. For the used chips, this distance mitigated capturing forming droplets and deforming droplets flowing into the wider section of the outlet where capturing distinct droplets could be jeopardized by the loss of gaps between droplets. The assembly was attached to the top of the 3 DoF chip mount (Section II-A-II-b and Fig. 2/2/b).

III. EVALUATION METHODOLOGY

In this section, we present the prototype system evaluation methodology used for characterization and benchmarking on a system as well as on a submodule level.

The first test series (Section III-A) focused on evaluation of system submodules or groups of submodules. Fine-tuning steps were also taken to prepare for the system integration. The second test series (Section III-B) focused on characterizing and benchmarking the integrated system prototype in droplet generation.

In all test setups, droplets were generated using fluids as described in TABLE 3.

In all test setups including a camera, a high-speed camera module (acA640-750uc, Basler) was used. The camera frames were captured in real time on the computer using Basler's pylon Viewer software.

A. SUBMODULE EVALUATION

The test setup used (Fig. 11/a) in this section was an early proof-of-concept implementation of the full experimental setup presented in Section II-A. The setup was derived from components demonstrated in our earlier works ([23], [24]). In the setup, DIW was used as the disperse phase, oil A or B as the continuous phase. Both phases were pumped into the droplet generation chip using our custom pumping system based on Bartels Mikrotechnik micropumps (mp6-liq). Results are presented in Section IV-A.

1) PRESSURE-BASED SYSTEM FEEDBACK MODELLING

Tests done with the following methodology gave results for: characterization of pressure control, definition of voltage to pressure transfer functions and tuned pressure feedback PID gains using the transfer functions.

TABLE 3. Fluid phases used in droplet generation experiments.

	A	B
Disperse phase	deionized water (DIW)	deionized water (DIW)
Continuous phase	Sigma-Aldrich 33079 mineral oil + 2% w/w surfactant (Span® 80, Sigma-Aldrich)	HFE 7500 fluorocarbon oil + 2% w/w surfactant (perfluoropolyether (PFPE)-poly(ethylene glycol) (PEG)-PFPE triblock)

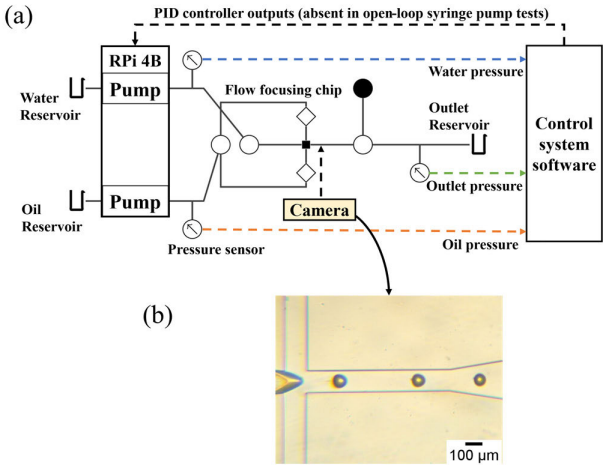

FIGURE 11. Schematic diagram for the experimental setup of droplet microfluidics system: (a) block diagram of the control system, (b) camera image of the droplet generator junction.

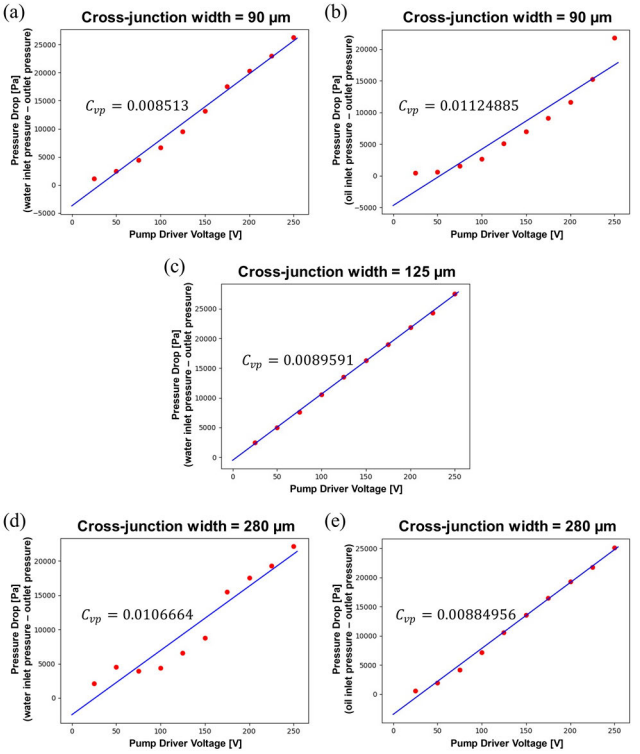

FIGURE 12. Pressure drops vs. peak-to-peak voltages of the piezoelectric micropump for the chip variants with cross-junction widths: 90 μm with DIW (a) and with oil A (b); 125 μm with DIW (c); and 280 μm with DIW (d) and with oil A (e). Driving frequency for water pump was 200 Hz sinewave. The driving voltage waveform was 200 Hz sinewave for the water pump and 50 Hz sinewave for the oil pump.

The pressures at the inlets and outlets of the microchannel were measured using Honeywell pressure sensors MPRLS0015PG0000SA and MPRLF0250MG0000SA, respectively, with a sampling rate of ∼166 Hz. To obtain pressure to pump driving voltage relationships, driving voltage tests were conducted. For three chip variants (relevant chip dimensions in TABLE 2), the driving voltage of the piezo pumps ranged from 25 V to 250 V, with a step size of 25 V. Corresponding pressures were recorded for a duration of one minute at each step with the steady state averaged as the resulting pressure value. Measurements were done separately for DIW and oil A. Unwanted transients or spikes in the experimental data were removed using median filtering (performed in MATLAB).

To tune the PID gains, experimental data (from our earlier works [21], [22]) demonstrating the effect of inlet pressure on droplet size were used in MATLAB to derive pumping system component transfer functions. The transfer functions were implemented in Simulink in a setup-derived closed loop feedback model. PID K-values were found among six objective function criteria obtained from using genetic algorithm method: the Integral Squared Error (ISE) criterion; the Integral Time Squared Error (ITSE) criterion; the Integral of Time Absolute Error (ITAE) criteria; the Integral of Absolute Error (IAE) criterion; the Mean Squared Error (MSE) criterion; the Integral Error (IE) criterion).

2) SYRINGE PUMP VS. PRESSURE-DRIVEN PUMP

As laboratories often use syringe pumps for droplet microfluidics, the performance of our pressure-based micropump system against syringe pumps was compared here.

Two syringe pumps (NetPump, SpinSplit LLC, Budapest, Hungary) with plastic syringes were used to pump oil A and DIW into chip variant A. Pressure sensors were set in the established configuration (Fig. 11/a). The syringe pumps were connected to local network via Ethernet and interfaced with SpinStudio (SpinSplit LLC, Budapest, Hungary) on a desktop computer. Droplet formation was observed using a camera, placed beneath the FFD's cross-junction. Syringe pumps were set to run for about four minutes, with fixed flow rates (Fig. 14/a), producing uniform droplets. One minute from the end of the steady state period of the measured oil and water pressure drops over the chip were averaged and used as targets for the pressure pump PIDs corresponding to the matching fluid phase. Followingly, the inlet tubes were disconnected from the syringe pumps and connected to the pressure pumps. For two minutes, pressure pumps were pumping oil and water with closed loop control, with comparable pressure (Fig. 14/b).

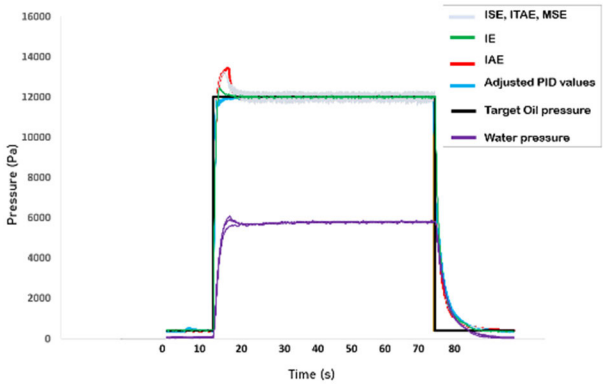

FIGURE 13. Simulation results for pressure feedback PID controller tuning with a genetic algorithm for oil pressure control.

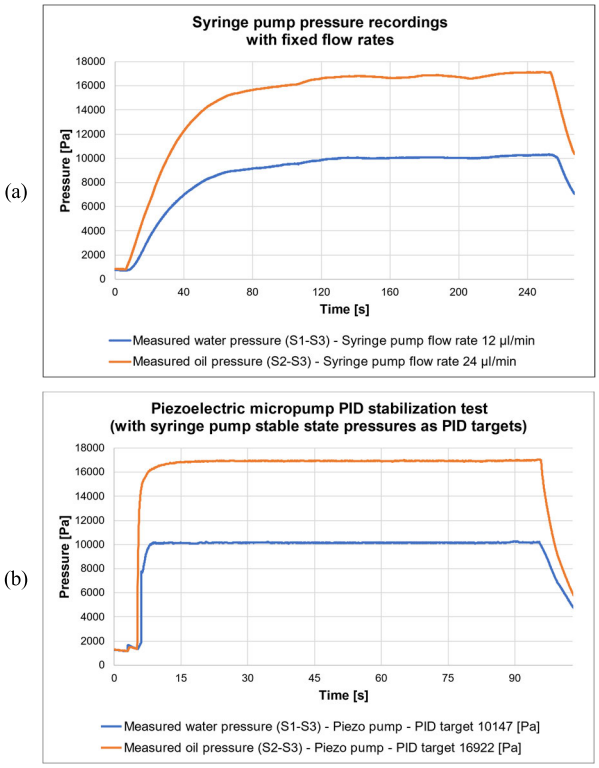

FIGURE 14. Pressure stabilization experiments performed on the setup shown in Fig. 11/a. Syringe pumps were set to pump with 12 μl/min for DIW and 24 μl/min for oil A. One minute period from the end of stable state pressures on (a) were averaged and used as pressure targets for the piezoelectric micropump PIDs. a) Responsiveness of flow-rate driven system (with third-party syringe pumps); b) Responsiveness of our pressure-driven system.

3) SENSORICS, PHOTODIODE VOLTAGE INTERPRETATION

Before droplet observations with a PD, a camera was used to analyze possible scenarios. Droplets were generated with DIW in separate combinations with oil A and B (TABLE 3). Droplets were recorded as image series to a computer and afterwards analyzed visually. Additionally, images of droplets were scanned through a custom pixel color summation program, used to estimate possible collectable waveforms from the PD. The custom program had an additional feature to roughly mimic a variable pinhole (determinable by the angle of the droplet generation chip in the chip mount).

4) SYSTEM CONTROLLER BENCHMARKING

The selected controller (RPI) had a quad core processor limiting concurrent tasks to four. Additionally, with RPI running a desktop OS, loop stability of each task, split using multiprocessing Python library, was measured in a one-time operation – finishing with complete termination processes. As this required all connected submodules, the test took place at the final stages of integration. All tasks running in parallel on RPI were timed over a 90 second droplet generation operation using chip variant C with oil B.

Furthermore, three additional 90 second tests were run (2 with chip variant C and 1 with chip variant B). After 45 seconds into the tests, ~3 seconds of ADC data (from task/core 3) was logged in more detail to analyze controller related latency and performance with a custom droplet interpretation algorithm. In the same period, a sample image was taken from the waveform entering the ADC, visualized on a connected oscilloscope (DSO5014A, Keysight).

B. SYSTEM EVALUATION

In system evaluation methodology, unless specified otherwise, oil B (TABLE 3) was used as the continuous phase.

1) DROPLET SIZE AND FREQUENCY CONTROL

For this evaluation process, two sets of target series tests (size and generation rate) were conducted for each of the two chip variants (B and C) – shown on TABLE 4–7. All samples in series were given 15 seconds for stabilization which was discarded from further calculations. The remaining 21 seconds for each sample was used for CV% and error calculations. Due to geometric differences between chip variants, target ranges of named series were limited to combinations more likely to produce droplets.

2) MEASUREMENT OF COEFFICIENT OF VARIABILITY OF GENERATED DROPLETS

To measure the stability of droplet generation with the proposed system, coefficients of variability (CV%) were calculated from "digitized" droplet data (relative droplet size over the photodiode as voltage and droplet generation rate as frequency from droplet-to-droplet period) obtained with specified droplet feedback PID targets after the setup was ran through the calibration algorithm described in ESI S3. CVs were calculated from voltage and frequency series obtained from dual-PID tests, allowing 15 seconds for stabilization at the start of each stage. This left 21 seconds of stabilized data on each target for CV calculation. CVs were also calculated from additional datasets made with longer stabilization (30 s) and stable periods (45 s). As generation frequency did not strictly apply to droplet length, CV of generation frequency was not combined with relative size CVs. However, droplet generation frequency target series were further quantitatively

TABLE 4. Chip B – voltage target series over fixed generation frequency targets.

	Fixed Generation Rate Target	Voltage / Size Target 1	Voltage / Size Target 2	Voltage / Size Target 3
1	200 Hz	2.0 V	2.8 V	3.6 V
2	400 Hz	2.0 V	2.8 V	3.6 V
3	600 Hz	2.0 V	2.8 V	3.6 V
4	800 Hz	2.0 V	2.8 V	3.6 V

TABLE 5. Chip B – frequency target series over fixed voltage (size) targets.

	Fixed Voltage / Size Target	Generation Rate Target 1	Generation Rate Target 2	Generation Rate Target 3	Generation Rate Target 4
1	2.0 V	200 Hz	400 Hz	600 Hz	800 Hz
2	2.8 V	200 Hz	400 Hz	600 Hz	800 Hz
3	3.6 V	200 Hz	400 Hz	600 Hz	800 Hz

TABLE 6. Chip C – voltage target series over fixed generation frequency targets.

	Fixed Generation Rate Target	Voltage / Size Target 1	Voltage / Size Target 2	Voltage / Size Target 3	Voltage / Size Target 4
1	200 Hz	3.2 V	3.4 V	3.6 V	~~3.8 V~~
2	300 Hz	3.2 V	3.4 V	3.6 V	3.8 V
3	400 Hz	3.2 V	~~3.4 V~~	~~3.6 V~~	~~3.8 V~~
4	500 Hz	3.2 V	~~3.4 V~~	~~3.6 V~~	~~3.8 V~~

TABLE 7. Chip C – frequency target series over fixed voltage (size) targets.

	Fixed Voltage / Size Target	Generation Rate Target 1	Generation Rate Target 2	Generation Rate Target 3	Generation Rate Target 4	Generation Rate Target 5
1	3.2 V	200 Hz	300 Hz	400 Hz	500 Hz	600 Hz
2	3.4 V	200 Hz	300 Hz	400 Hz	500 Hz	600 Hz
3	3.6 V	200 Hz	300 Hz	400 Hz	~~500 Hz~~	~~600 Hz~~
4	3.8 V	200 Hz	300 Hz	400 Hz	~~500 Hz~~	~~600 Hz~~

analyzed via standard deviations and CVs (further detailed in ESI S4). Multiple CV sets were required for observing the impact from droplet generation frequency, pumping frequency (as piezo pump driving frequency) and average pressure in the chip to droplet size CV.

In addition, to attest to the meaning and comparability of voltages obtained from the photodiode, claimed as corresponding to droplet size, visual data of droplets was needed. For visual data, droplets, generated with fixed pressure targets, were collected into an Eppendorf Tube® to be measured afterwards. Imaging for measurements was done with a trinocular microscope (BX61, Olympus) using a camera (DP70, Olympus) and a 4x/0.16 lens (UPLSAPO, Olympus). CVs and averaged cross-sectional areas and diameters were calculated using ImageJ software (further described in ESI S5). For better viewing, droplets were pushed into Countess™ Cell Counting Chamber Slides (ThermoFisher) with a channel height of 100 μm.

IV. EVALUATION RESULTS AND DISCUSSION

In all tests, droplets were generated with liquids following the naming scheme given in Section III.

A. SUBMODULE EVALUATION

1) PRESSURE-BASED SYSTEM FEEDBACK MODELLING

With the ramping pump driving voltage (25 V to 250 V) tests, linear correlation between voltage and pressure generated in tests with all chip variants were observed (Fig. 12). The relationship of pressure drops across the chip to pumping voltages varied for the different chip variants. This was quantified with the voltage-to-pressure coefficient (C_{vp}). Furthermore, while the rising trend of the C_{vp} of water tests was rising

along with the cross-junction width, the ratio of water and oil C_{vp} was different between chips with different oil entry angles (Fig. 12/a-b vs. Fig. 12/d-e). The coefficients obtained with chip A were used in the controller design to account for differences in junction widths.

Based on our earlier works [21], [22], the system components were mathematically represented as transfer functions in eqns. 1-3, using the collected data in MATLAB software.

$$\text{t.f.}_{\text{pwat}} = \frac{-17.42s + 83.92}{s + 0.69} \tag{1}$$

$$\text{t.f.}_{\text{poil}} = \frac{-8.40s + 30.6123}{s + 0.216} \tag{2}$$

$$\text{t.f.}_{\text{chip90}} = \frac{19.04s + 0.339}{s + 0.275} \tag{3}$$

where $\text{t.f.}_{\text{pwat}}$ is the transfer function of the water pump, $\text{t.f.}_{\text{poil}}$ the transfer function of the oil pump, and $\text{t.f.}_{\text{chip90}}$ the transfer function of the chip variant A. From Simulink results the controller parameters with the lowest fitness values (error) were chosen for real-world experiments. PID's K_p, K_i, K_d values for water pump (10.5, 60.77, 1.64e5), obtained from the IE objective function, resulted in good long-term stability, albeit with an overshoot, whereas K_p, K_i, K_d values (6.69, 46.10, 5.81e-5), obtained from the IAE objective function, resulted in a response with negligible overshoot, but instead with oscillations around the target value. Based on the comparison of GA tuning results (Fig. 13), manual adjustments to K_i were made to prevent overshoot and maintain good stability, with new K_p, K_i, K_d values (10.5, 17.5, 5.81e-5) for water. Following the same process, K_p, K_i, K_d values were found for oil (40.0, 18, 4.78e-4).

2) SYRINGE PUMP VS. PRESSURE-DRIVEN PUMP

The pressure stabilization and steady states of the two test scenarios described in Section III-A-II are shown in Fig. 14. Syringe pumps took approximately 120 seconds to reach a reasonable steady state for new pressure targets, with minor oscillations persisting. Slower response time for syringe pumps was attributed to linear operation of the motors' speeds, however, the likely cause for persistent oscillations was attributed to inconsistent friction of the syringe's rubber gasket. In comparison, pressure-driven micropumps showed better responsiveness and stability between changing input pressure targets, taking about 10 seconds to reach the defined inlet and outlet pressure values.

The faster response rate helped significantly reduce experiment runtimes and reagent waste during the system evaluation tests (Section IV-B, e.g., exploring ranges of producible droplet sizes and generation rates).

3) SENSORICS, PHOTODIODE VOLTAGE INTERPRETATION

While generating droplets using oil A, the formed droplets (Fig. 15) indicated that once the droplet's diameter exceeded the larger dimension of the channel (Fig. 15/c), the shadow caused by refractions in the phase transition region would intensify. Furthermore, a central low refraction region would emerge.

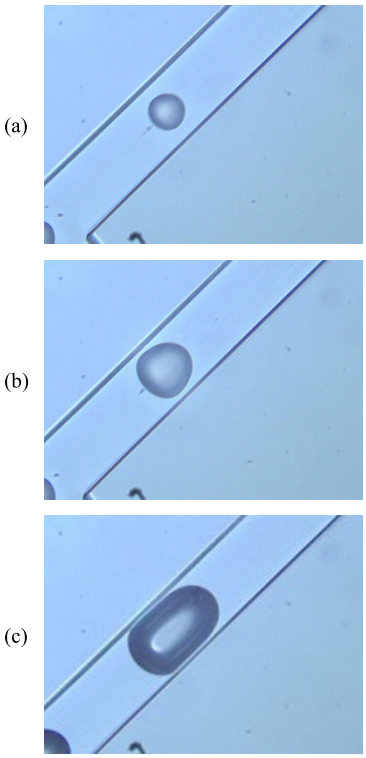

FIGURE 15. Recorded camera images of droplets generated with DIW and oil A in a 125 μm wide microfluidic channel taken at 555 frames per second under brightfield LED. a) ~58.4 μm length droplet, generated with 5.2 kPa and 11.0 kPa for water and oil pressures respectively; b) ~112.7 μm length droplet, generated with 5.2 kPa and 9.5 kPa for DI water and oil A pressures respectively; c) ~182.0 μm length droplet, generated with 5.2 kPa and 7.5 kPa for water and oil pressures respectively.

The possible impact of the low refraction region on the captured photodiode light intensity waveform was estimated from the custom pixel color summation program (Fig. 16). Given the fixed size moving window on Fig. 16/a-c, it was noted, that even with a longer than ''window size'' droplet, whose diameter was less than the larger dimension of the channel (Fig. 16/b), the estimated waveform gained little to no distortions. Mild distortion could be attributed to the bullet-like shape of the droplet. However, a much more noticeable distortion was noted once the low refraction region became significant relative to the window size. The non-phase transition region had the potential to invert the tip of the waveform. The impact of this effect was amplified with a less viscous continuous phase, as that reduced the surface tension of the droplet and the intensity of the droplet's shadow along with it.

Using oil B for the continuous phase, generated droplets showed inherently thinner phase transition regions and gave way for larger low refraction regions (Fig. 17). The images show a case where not only was the phase transition region very thin, but the aligned droplet acted like a lens (Fig. 17/c). To further inspect the impact of such cases, consecutive

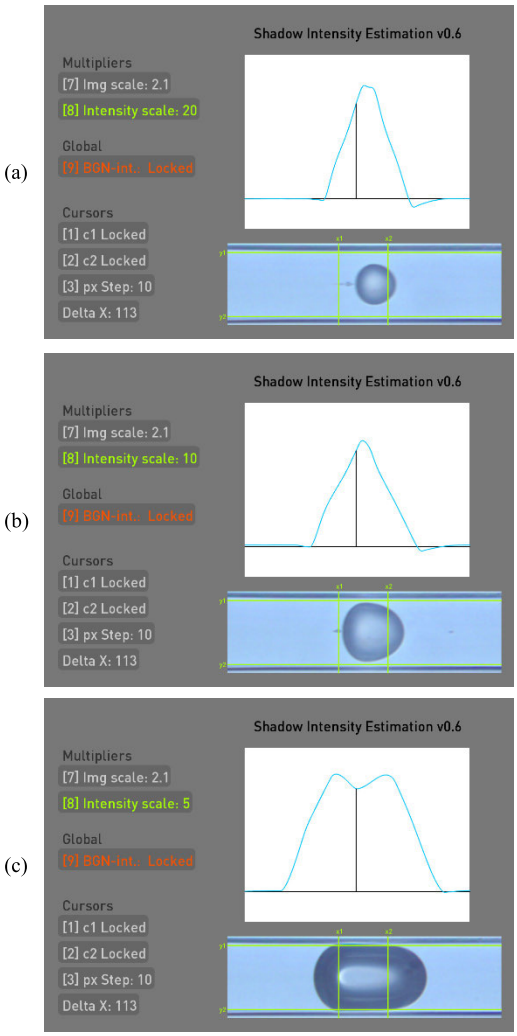

FIGURE 16. Rotated and cropped camera images shown in Fig. 15, respectively, were scanned with a fixed size moving window, indicated by green vertical lines to obtain corresponding intensity graphs (blue waveform above droplet image). a) low-distortion triangular waveform produced by the ∼58.4 μm length droplet with a relative intensity multiplier of 20.0; b) low-distortion triangular waveform produced by the ∼112.7 μm length droplet with a relative intensity multiplier of 10.0; c) high-distortion trapezoidal (double-peak) waveform produced by the ∼182.0 μm length droplet with a relative intensity multiplier of 5.0.

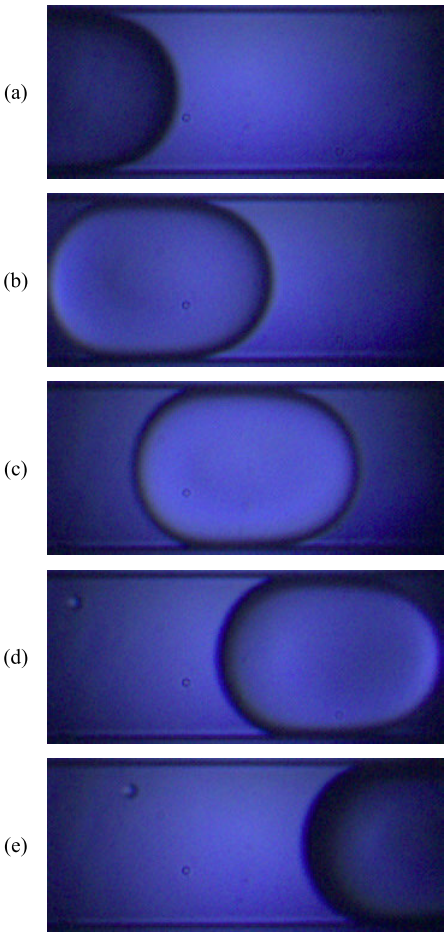

FIGURE 17. Cropped recorded frames of a passing droplet during generation with oil B. Droplet was generated at 5.0 kPa and 5.5 kPa water and oil pressures respectively. Displayed droplet measures ∼171.9 μm in length and was recorded at 1810 frames per second. A circular ∼190 μm diameter pinhole was used under the microfluidic chip below the recorded region to improve the visibility of the droplet. a) reference frame 1 in series, droplet entering the pinhole aperture; b) reference frame 2 in series, droplet approaching the center of the pinhole aperture; c) reference frame 3 in series, droplet in the middle of the pinhole aperture; d) reference frame 4 in series, droplet leaving from the center of the pinhole aperture; e) reference frame 5 in series, droplet exiting the pinhole aperture.

frames were viewed in the custom pixel color summation program (Fig. 18). Due to the usage of a pinhole, the extra shadows at the edges (background noise) were subtracted from further intensity calculations using the 6th additional frame (Fig. 18/f). Seen from Fig. 18 with a droplet, sized large enough to be squished in the microfluidic channel, flowing in low viscosity oil B, the possible recorded waveform for a single droplet could resemble a much more severe case of Fig. 16/c – instead of a slightly dipping peak, a waveform section representing a single droplet with a possible dip as low as to split into two discernible droplets.

4) SYSTEM CONTROLLER BENCHMARKING

Individual task duration details can be seen on TABLE 8. Maximum loop durations of the waveform interpretation and pumping pressure target calculation tasks (marked with * in TABLE 8) were caused by spikes in OS latency. Noticeably longer than average maximum loop durations for the remaining tasks were caused by delays from communication termination procedures included in the timing of the last loop. Total durations of tasks other than the pumping pressure target calculation task, where the main operation timer was running, were longer due to beginning their termination process after the defined 90 s time limit. Their difference was caused by sequential termination process (some extending for multiple seconds due to large log file generation). For droplet waveform interpretation task, the average loop duration extended to ∼6.5 μs, resulting in a mean sampling rate of ∼153 kHz. The discrepancy between minimum loop duration of pump communication task (∼15 ms) and pump

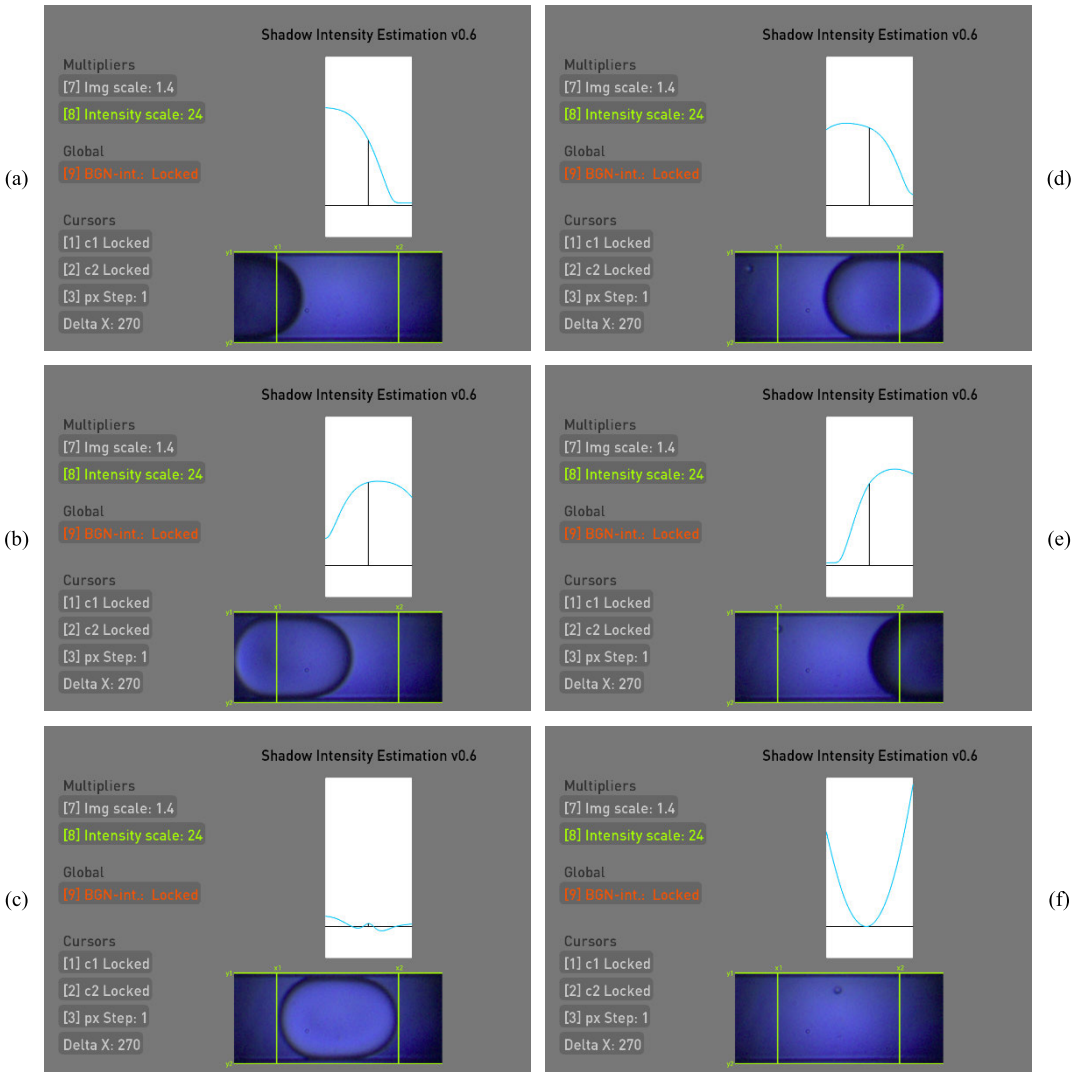

FIGURE 18. Camera images shown in Fig. 17, respectively, and an extra 6th frame were scanned with a fixed size moving window, indicated by green vertical lines to obtain corresponding intensity graphs (blue waveform above droplet image). All intensity graph scaling multipliers were kept at 245.0 for better visualization and comparability. The intensity of the 6th frame, representing the background noise, was recorded first, and locked into memory. Background intensity was subtracted from the following calculations. a) Indicating a rising shadow intensity as the darkest region of the droplet entered the pinhole aperture and the moving window; b) indicating a past-peak shadow intensity as the droplet moved closer to the center of the pinhole aperture and the moving window; c) indicating the lowest shadow intensity while the droplet was positioned at the center of the pinhole aperture; d) indicating an approaching-peak shadow intensity as the droplet was leaving the central region of the pinhole aperture and the moving window; e) indicating a falling shadow intensity as the darkest region of the droplet was exiting the pinhole aperture and the moving window; f) indicating the intensities of the shadows at the edges of the frame, caused by the pinhole.

TABLE 8. Controller software's task loop duration.

	Core 1 – User interface coms. (Section II-B-3-1)	Core 2 – Pumping system coms. (Section II-B-3-2)	Core 3 – Droplet interpretation (Section II-B-3-3)	Core 4 – Droplet PID calculations (Section II-B-3-4)
Maximum [ms]	203.4370	215.0430	20.25914*	21.05400*
Average [ms]	102.0334	18.98948	0.006515	0.169749
Minimum [ms]	100.6310	14.74400	0.002861	0.104000
Loops counted	1005	4 758	14 640 000	530 200
Total [s]	102.54	90.35	95.38	90.00

sensor update rate of ∼166 Hz (6 ms) was attributed to having used asynchronous communication method.

In the OS latency and droplet interpretation algorithm impact analysis, droplet waveform from the first additional

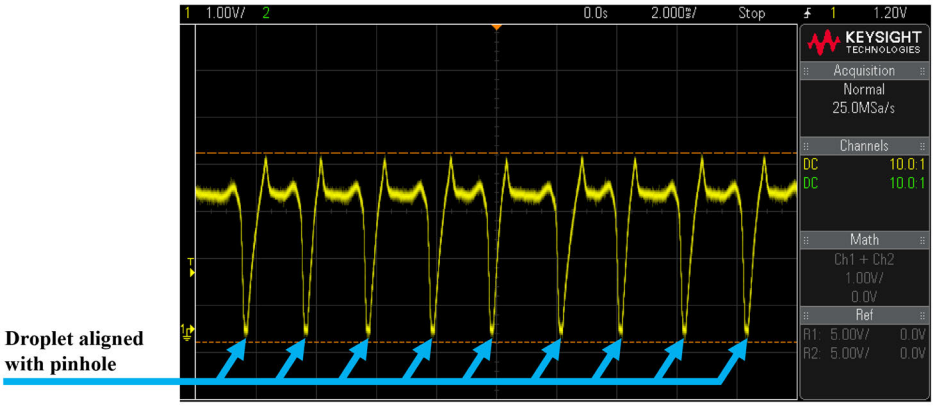

FIGURE 19. Oscilloscope screen capture of recorded amplified, inverted photodiode voltage during droplet generation with chip variant C, at a rate of ∼500 Hz. Droplet alignment with the pinhole noted with blue arrows (at the "troughs"). Instability in the droplet production rate is recognizable by the varying time gaps between the „troughs".

test with chip variant C (Fig. 19) indicated that the pinhole-aligned droplets were seen as an increase in light intensity. Meaning that the droplets functioned as lenses instead of obstacles. In this scenario, the ''peak'' of the alignment was measured at the ''trough''. Each ''trough'' could be imagined as a more severe form of the dip shown in Fig. 16/c. Each ''trough'' was accompanied by its darker incoming and outgoing edges (Fig. 18/a, 18/e). From the logged ADC data, a sample section (Fig. 20) showed the limits of RPI running code written in Python on a non-real-time OS and specific functions circumstantially interacting poorly with the OS. As the average ADC task loop duration was measured around ∼6.5 μs (TABLE 8), Python's multiprocessing Queue functions empty() and get_nowait(), called after 100 mV above the average line for every other droplet, delayed the loop duration minimally another ∼100 μs producing erroneous droplet size measurements. In comparison, the second test with chip variant C (Fig. 21) showed a waveform with similar sharp peaks, but each with longer duration. Long enough to preserve the peaks captured by the ADC (Fig. 22). In the third additional test, with chip variant B, OS latency was spotted causing the loss of 2-3 consecutive droplets (Fig. 23) with an unexpected delay between two ADC sampling cycles. Albeit being relatively rare, the measurement error of such events was mitigated to prevent destabilizing the flow rates. When time delay between two ADC samples exceeded 30% of the average droplet generation period, the following erroneous droplets were excluded from the logs and use in the droplet feedback PIDs. It improved fluidic stability, but in the case of random OS delays, at the cost of up to 10% of generated droplets not getting logged (losses were lower with lower generation rates). Likewise, in the case of get_nowait() delay, if it exceeded 30% of the average droplet generation period, the irregular droplet measurement would be excluded from the log and PID feedback.

B. SYSTEM EVALUATION

After assembly, programming, and fine-tuning through preliminary testing, connection between a laptop and the CogniFlow-Drop device was established through a Wi-Fi hotspot to validate the communication interface. After a successful connection, the interface effectively transmitted and received message packets every ∼100 ms, artificially delayed with eCAL message polling delay on the RPI. Other functional tests with the remote control included:

- initiating setup calibration (tied to variables: chip position/angle, chip variant, liquids used),
- initiating droplet generation with desired size and generation rate,
- initiating droplet size (V) target series test,
- initiating droplet generation rate (F) target series test.

Each feature of the GUI (Fig. 8) was proceeded to be used as remote initiator for the following system evaluation steps.

1) RESULTS OF DROPLET SIZE AND FREQUENCY CONTROL TEST SERIES

During experimentation, some target droplet size and generation frequency combinations did not yield droplets regardless of having used selective ranging – highlighted on TABLE 6-7. Overall, chip C showed lower ranges for both sizes and generation rates. Additionally, chip C behaved uniquely between voltage and frequency series, as the combination of (400 Hz; 3.4 V) in voltage series did not yield droplets, but in contrast, was unexpectedly stable in frequency series. This hinted to higher sensitivity to size target alterations during droplet production combined with how current droplet feedback PID handles high instability.

Target series over all four sets, named in Section III-B-I, resulted in averaged droplet size errors, seen on Fig. 24, which indicated higher accuracy for droplet size control with chip B, more specifically with droplet size (V) series when the marked outlier of ChipB-Fseries was taken into account. With an average error of -0.06%, ChipB-Vseries obtained averaged sizing errors between +2.86 to -1.79%. Contrast of accuracy of reaching average target size, can be seen on droplet capture graphs between ChipB-Vseries (row 4 from TABLE 4) and ChipC-Vseries (row 2 from TABLE 6) on Fig. 24/b and Fig 24/c respectively, with target sizes per sample,

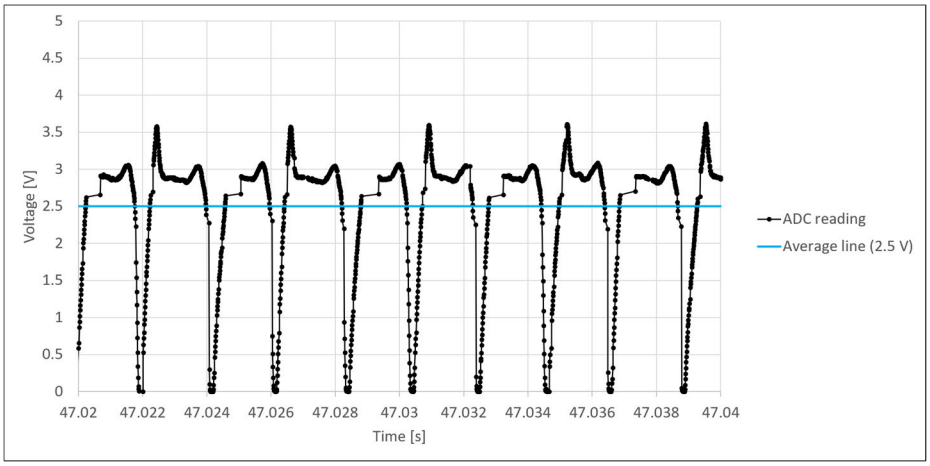

FIGURE 20. Sample frame from ADC measurement log on RPI showing ADC readings and the average line over which droplet detection was handled. Shown graph links with Fig. 19, however, with every other peak cut off due to specific cross-core communication function delays.

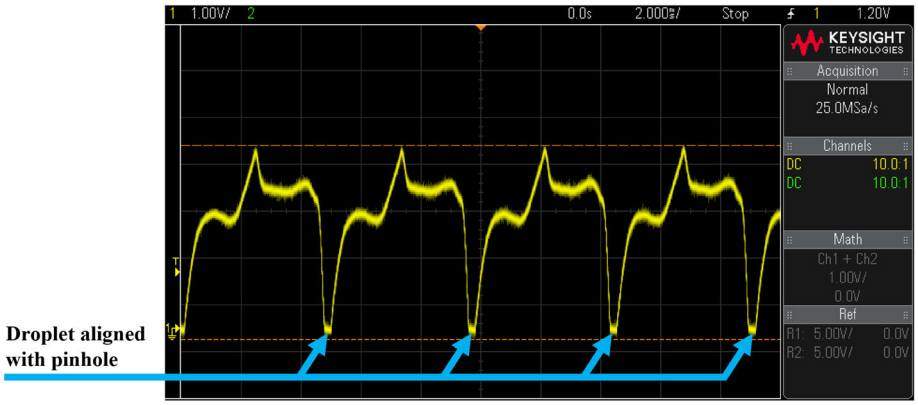

FIGURE 21. Oscilloscope screen capture of recorded amplified, inverted photodiode voltage during droplet generation at a rate of ∼200 Hz. Droplet alignment with the pinhole noted with blue arrows (at the "troughs").

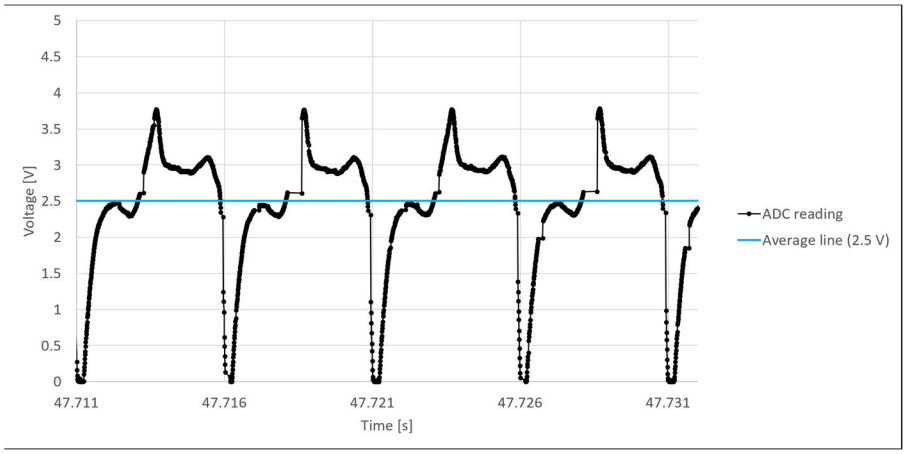

FIGURE 22. Sample frame from ADC measurement log on RPI showing ADC readings and the average line over which droplet detection was handled. Shown graph links with Fig. 21, however, in contrast to Fig. 20, cross-core function delays caused after every other detected droplet, were not long enough to cut off the relevant peaks of the droplet waveform.

segmentally overlayed as orange horizontal lines. Target size errors on Fig. 24/b were [+0.35; -1.79; -1.56] % respectively. Together with the fixed frequency (200 Hz) accompanied with varying droplet size targets, frequency errors of [+0.88; −2.00; −5.63] %, respectively, showed a decreasing total output volume with the combined error staying further and

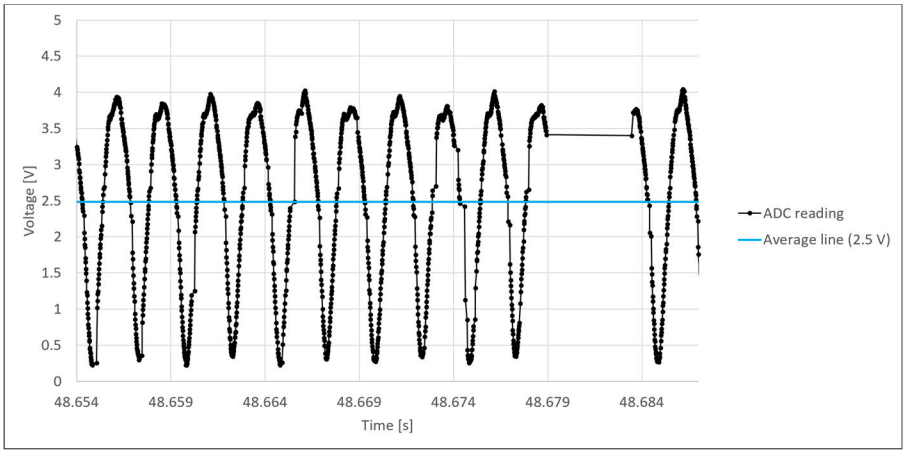

FIGURE 23. Sample frame from ADC measurement log on RPI showing ADC readings and the average line over which droplet detection is handled. In shown example, spontaneous latency delays caused by the operating system running on RPI prevented three consecutive droplets being captured and measured.

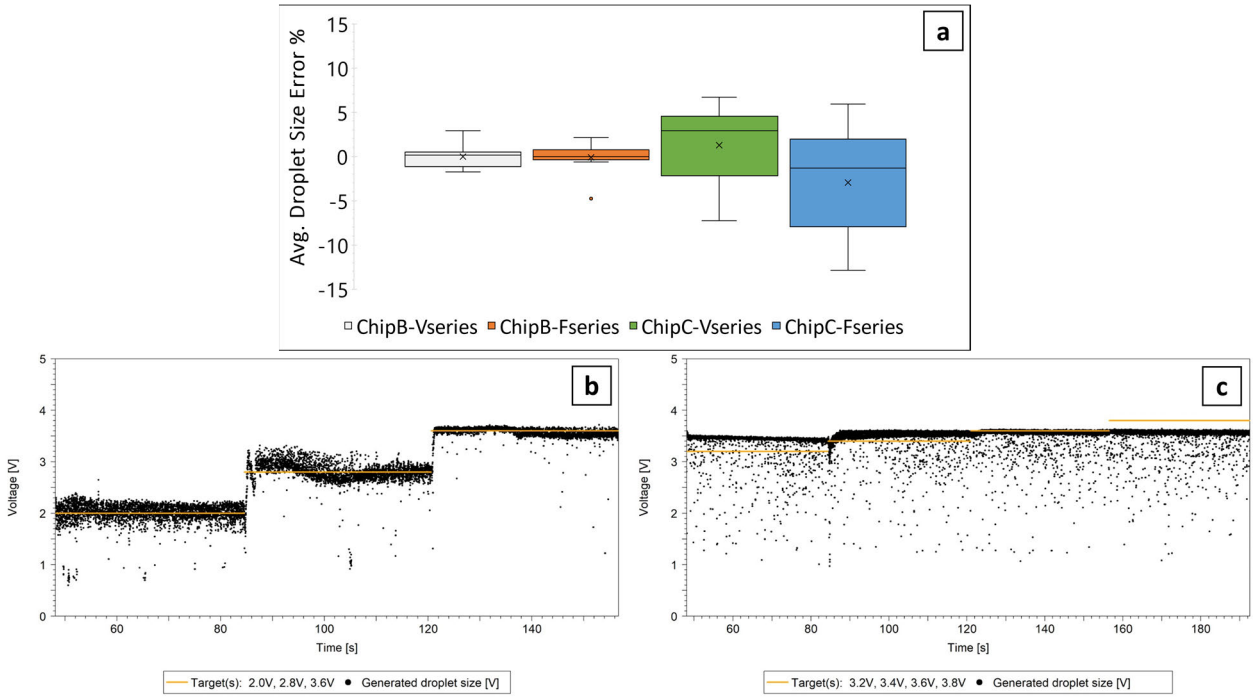

FIGURE 24. Results from Section IV-B-I. a) Averaged droplet size target errors for chips B and C, further split by size and frequency series test sets. Sample sizes for series respectively [12, 12, 9, 16]; b) Droplet size control dataset of row 1 from TABLE 4, from ChipB-Vseries test set. Graph indicating higher accuracy of stabilization around target voltage levels; c) Droplet size control dataset of row 2 from TABLE 6, from ChipC-Vseries test set. Graph indicating lower accuracy of stabilization around target voltage levels, preference to droplet size (influenced by chip geometry).

further below the targets. Target errors on Fig 24/c were [+5.62; +2.88; −2.03; −7.24] % respectively. For the comparably reduced functional size range that channel geometry of chip C offered, target size control did not yield droplets in all requested sizes. This could largely be contributed to inclinations caused by the channel geometry. This was made clear from its accompanied averaged frequency target errors of [−1.99; +2.65; −0.73; −0.30] % respectively, which did not follow the pattern of size errors. The secondary contributor was attributed to the erroneous droplet size averaging caused by what was shown on Fig. 20. Due to alterations in perception of captured droplet sizes, calibration for chip C test series had been segmentally impacted where droplet waveforms exhibited shapes more predisposed to peak losses.

Additionally, averaged droplet generation rate errors, seen on Fig. 25/a, again indicated higher accuracy for droplet rate control with chip B, more specifically with generation rate (F) series when marked outliers of ChipC-Fseries were taken into account. With an average error of +0.94%, ChipB-Fseries obtained averaged generation rate errors between +3.62 to −1.65%. Contrast of accuracy between the best and the worst captured series of reaching average target generation rate, can be seen on droplet capture graphs between

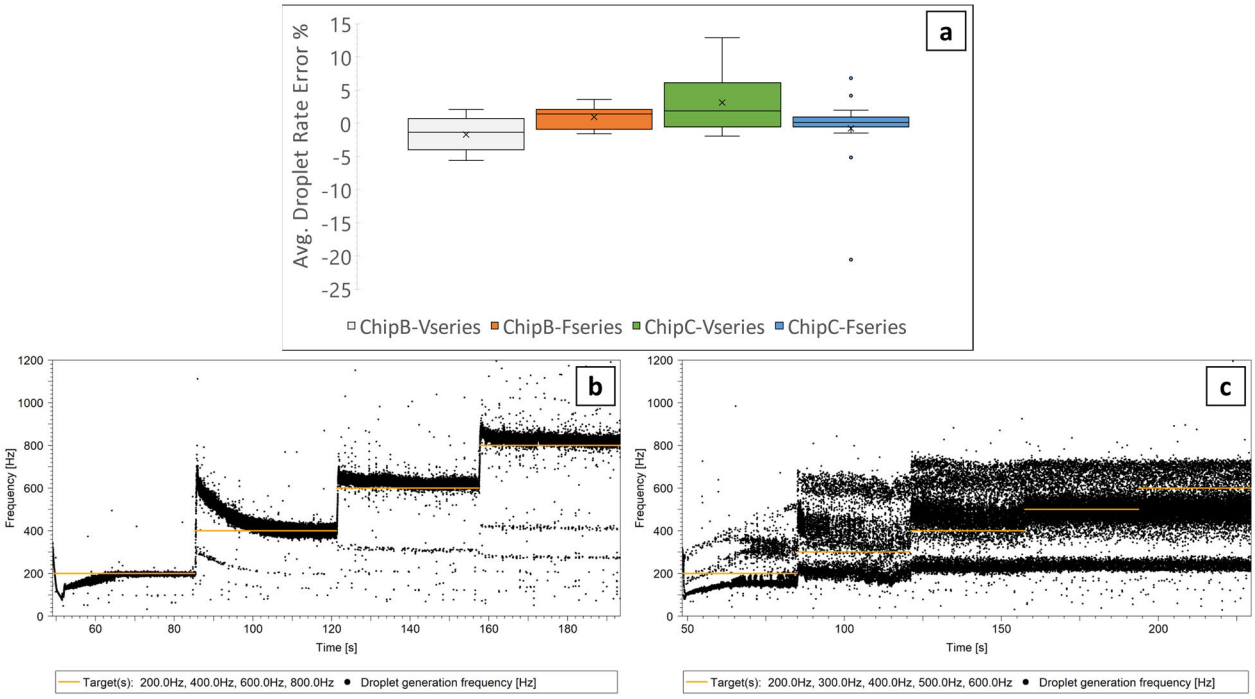

FIGURE 25. Results from Section IV-B-I. a) Averaged droplet rate target errors for chips B and C, further split by size and frequency series test sets. Sample sizes for series respectively [12, 12, 9, 16]; b) Droplet generation rate control dataset of row 2 from TABLE 5, from ChipB-Fseries test set. Graph indicating higher accuracy of stabilization around target frequency levels; c) Droplet generation rate control dataset of row 1 from TABLE 7, from ChipC-Fseries test set. Graph indicating lower accuracy of stabilization around target frequency levels and significant fluctuation in periodicity of droplet production.

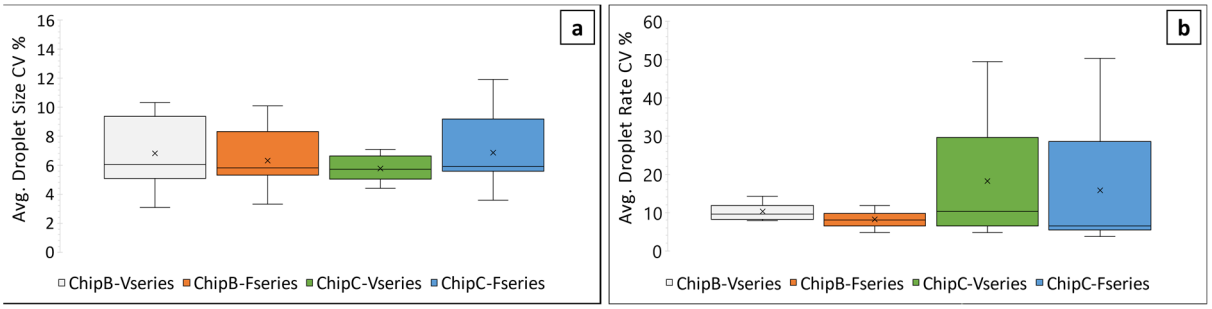

FIGURE 26. Results from Section IV-B-II. a) Averaged droplet size CVs for chips B and C, further split by size (V series) and frequency (F series) series test sets; b) Averaged droplet generation rate CVs for chips B and C, further split by size (V series) and frequency (F series) series test sets. Sample sizes for series respectively [12, 12, 9, 16].

ChipB-Fseries (row 2 from TABLE 5) and ChipC-Fseries (row 1 from TABLE 7) on Fig. 25/b and Fig. 25/c respectively, with target sizes per sample, segmentally overlayed as orange horizontal lines. Target averaged frequency errors, with chip B, on Fig. 25/b were [−1.43; +0.86; +1.83; +1.67] % respectively. Together with the fixed size target (2.8 V) accompanied with the example varying frequency targets, averaged size errors of [+0.50; −0.61; +0.61; +0.14] % respectively, showed no explicit relationship between size and frequency errors. This alluded to lesser impact from frequency alterations during droplet generation, in other words, lesser impact from changes in oil pressure rather than water pressure. Target averaged frequency errors, with chip C, on Fig. 25/c were [+1.93; +4.11; +6.78; −5.11; −20.61] % with accompanying size target (3.2 V) errors of [+5.91; −0.06; −1.56; −1.09; −1.13] %, respectively, showing little correlation in comparison. This example showed large fluctuations in periodicity, but small droplet size variation (similar to Fig. 24/c from ChipC-Vseries).

2) MEASUREMENT RESULTS FOR COEFFICIENT OF VARIABILITY OF GENERATED DROPLETS

a: DROPLET SIZE DATA (PD VOLTAGE DISCRETIZED WITH THE ADC) FROM CONSECUTIVE DROPLET SIZE AND FREQUENCY TARGET SERIES

V and F series performed in Section IV-B-I resulted in averaged droplet size CVs represented on Fig. 26/a and averaged

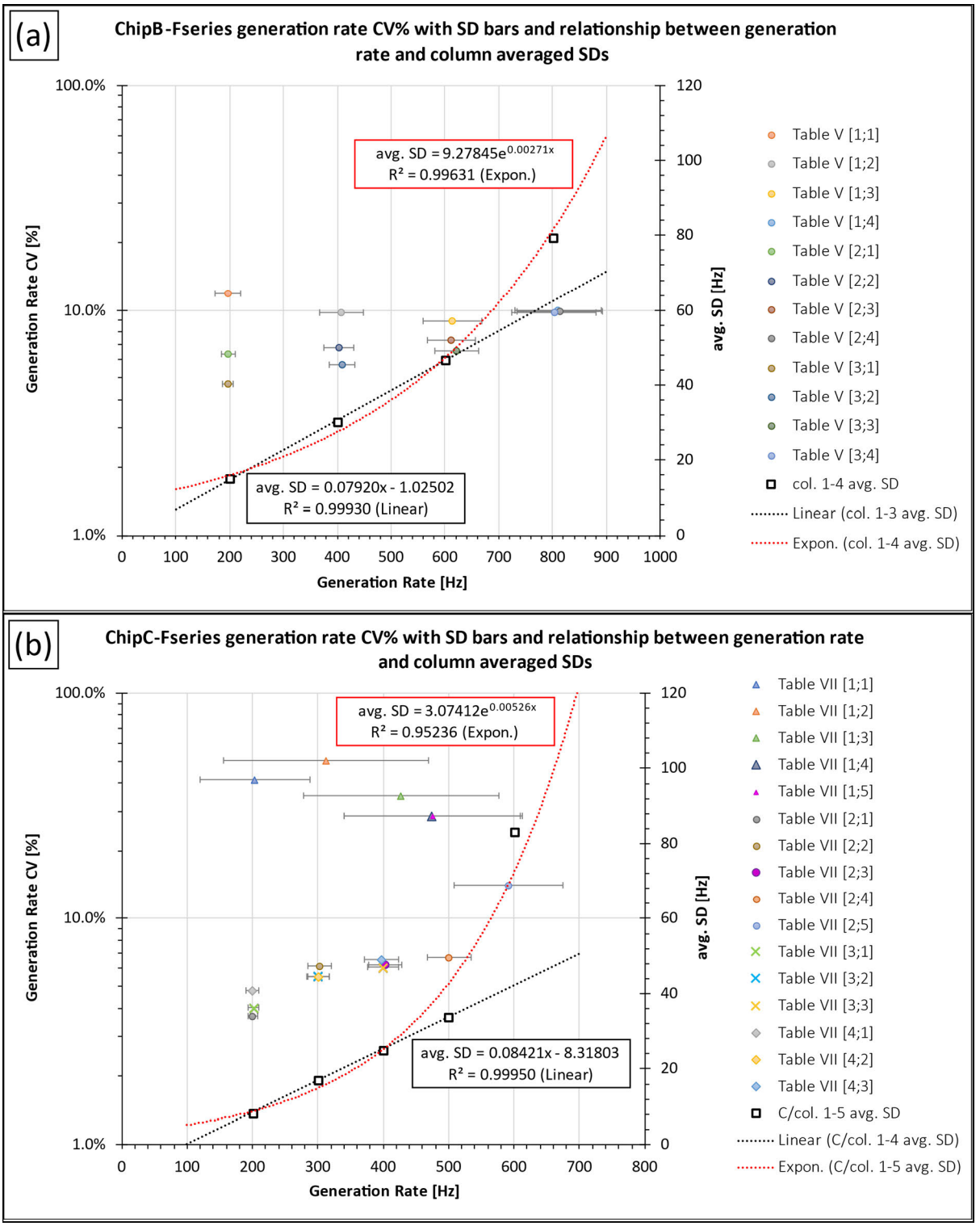

FIGURE 27. Results from Section IV-B-II. Quantitative analysis of F series data. a) Droplet generation rate CV%, from droplet size and rate combinations in TABLE 5, plotted against averaged generation rate, calculated over the stabilized generation period. TABLE 5 column (col.) averaged SDs (from target rate columns 1 to 4 and target size rows 1 to 3) plotted against column target generation rates together with a corresponding exponential regression line. Col. avg. SDs were cropped to columns 1 to 3 to highlight the highly linear correlation region; b) Droplet generation rate CV%, from droplet size and rate combinations in TABLE 7, plotted against averaged generation rate, calculated over the stabilized generation period. TABLE 7 column conditionally (C/col.) averaged SDs (from target rate columns 1 to 5 and target size rows 2 to 4 – row 1 conditionally excluded due to indicating a different mode of operation, see ESI S4 for details) plotted against column target generation rates together with a corresponding exponential regression line. C/col. avg. SDs were cropped to columns 1 to 4 to highlight the highly linear correlation region.

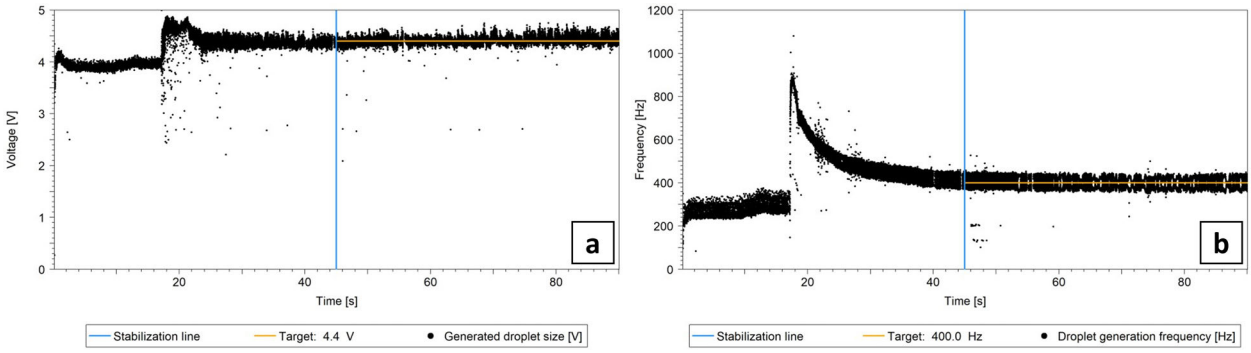

FIGURE 28. Results from Section IV-B-II. a) Droplet size target data set from a combination of [4.4 V; 400 Hz] with chip B. Stabilization period 45 seconds which includes an initial 15 seconds of default initiation period. Stabilization and stable segments are separated by blue vertical line. Target size in voltage is shown with an overlayed horizontal line; b) Droplet generation rate target data set from a combination of [4.4 V; 400 Hz] with chip B. Stabilization period 45 seconds which includes an initial 15 seconds of default initiation period. Stabilization and stable segments are separated by blue vertical line. Target size in voltage is shown with an overlayed horizontal line.

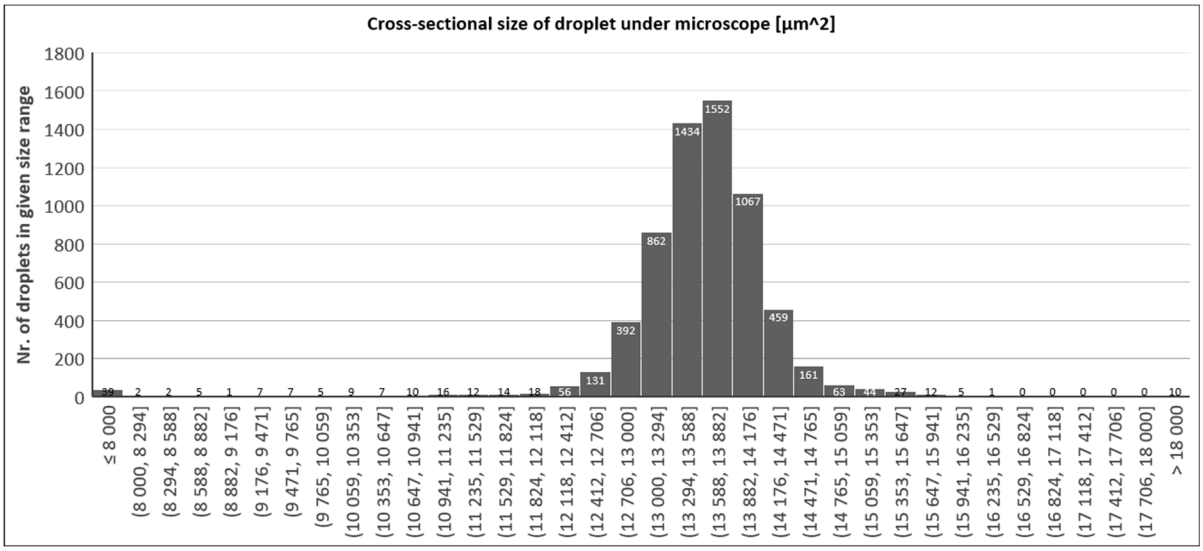

FIGURE 29. Droplet cross-sectional size spread from a droplet generation sample, generated with fixed water and oil pressure of 9 kPa and 12 kPa respectively. 6429 droplets measured over 11 images with ImageJ software.

droplet generation rate CVs represented on Fig. 26/b. Medians of averaged CVs from Fig. 26/a, [6.83; 6.33; 5.78; 6.84] %, respectively, showed that while the measured droplet sizes in tests with chip C were off noticeably more than with chip B, the size stability can be better. However, minimum CVs [3.10; 3.30; 4.40; 3.60] % showed favorability towards chip B. While some maximum CVs reached over 10%, more significant reasons for the larger instabilities stemmed from the chosen pressure combinations working less favorably with chosen chip geometries. From the averaged droplet generation rate results on Fig. 26/b, the difference between chip B and C was hard to mistake. As the CVs between size and rate for chip C, have a noticeable difference in scale, it was evident that the generation frequency of droplets does not inherently link to droplet size in a pulsatile pressure-based pumping system.

Further analysis of target F series provided relationships between the generation rate to generation rate CVs at each obtained average frequency level with standard deviation (SD) bars and between the target generation rate to column averaged SDs (SD averaging for chip C was done conditionally, further explained in ESI S4), for chips B and C respectively on Fig. 27/a and Fig. 27/b (numeric details in ESI S4, TABLE 1-4). Generation rate CVs for chip C revealed behavioral outliers with target size and rate combinations in row 1 of TABLE 7 (while producing droplets in a stable manner with size CVs $< 10\%$, the frequency CVs were well above 25%). By omitting the TABLE 7 row 1 CVs and SDs from comparison between chip variants, the general rule of increasing SD with increasing generation rate becomes noticeable. By having excluded row 1 SDs also from averaging of SDs, chip B and C generation rate averaged SDs ($\overline{SD}$) showed analogous trends. Both show the highest correlation to exponential relationships. Additionally, for both chip types, cropped $\overline{SD}$s revealed high linear correlation regions up to the second highest tested respective generation rate targets (Fig. 27) which in terms of generation rates would narrow down on the stable frequency region of use for that specific

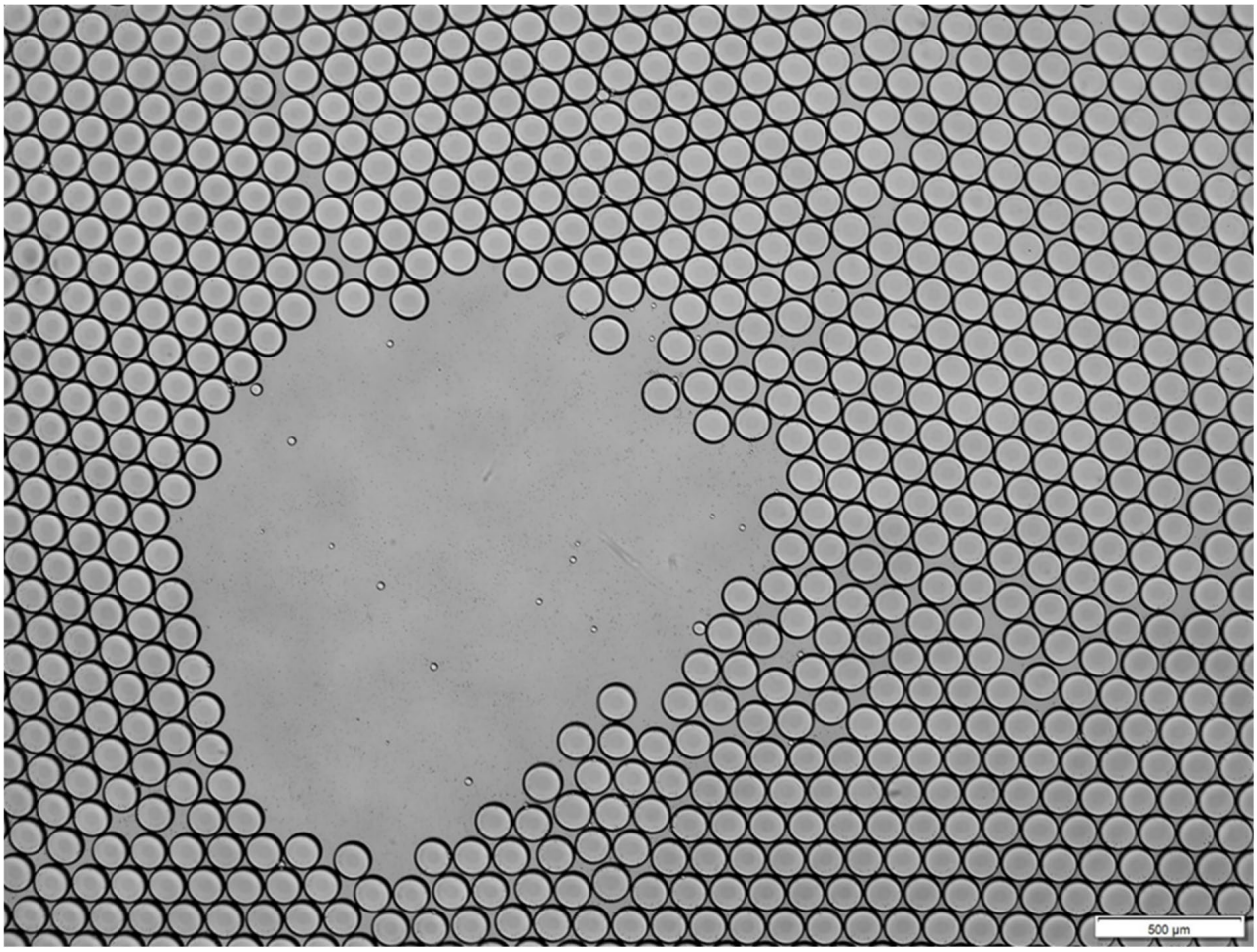

FIGURE 30. Droplets generated with chip design B with fixed water and oil pressures of 9 kPa and 12 kPa respectively, pumped using pressure-based piezoelectric micropumps, viewed under microscope (4x/0.16 lens).

chip geometry and fluidic phase combination. Between the observed initial and cropped data, beyond a certain generation rate, the behavior of frequency stability deteriorates from linear into exponential regime. The possible causes of which could be 1) stability limits, inherited from FFD channel design in combination with pulsatile flow and fluid phase properties, 2) hardware and/or software limits, RPI's droplet interpretation loop delays introducing increasing number of erroneous readings.

b: DROPLET SIZE DATA (PD VOLTAGE DISCRETIZED WITH THE ADC) FROM SINGLE SHOT DROPLET SIZE AND FREQUENCY TARGETS

Using chip B with different calibration (chip position slightly tilted in the light tower), one of the better examples with lowest target error in combination with the lowest droplet size CV (400 Hz, 4.4 V) achieved, can be seen on Fig. 28 with graphed droplet sizes and generation rates respectively. From the size dataset on Fig. 28/a, the CV% was calculated to be 1.77% with a percentage error from target droplet size of +0.27%. From frequency dataset on Fig. 28/b, the CV% was calculated to be 6.67% with a percentage error from target droplet generation rate of +0.22%.

c: DROPLET SIZE DATA (MICROSCOPE CAMERA ➜ IMAGEJ) FROM SINGLE SHOT PRESSURE TARGETS

Droplets were collected from tests with droplet feedback PIDs disabled to obtain a baseline. Tests were done with fixed water pressure at 9 kPa and several oil pressure targets in the range of 9 kPa – 12 kPa, ran over 90 seconds, where oil pressure at 12 kPa yielded the best results with 7.7% CV, with a spread of cross-sectional areas shown on Fig. 29. Average cross-sectional surface area of recorded droplets was measured 13 558.9 μm^2, translating into an average planar diameter of 131.4 μm when droplets were flattened in the imaging slide. A sample from a series of images taken of droplets in the droplet imaging slide can be seen on Fig. 30.

V. FUTURE PERSPECTIVE

One of the core principles of the CogniFlow-Drop system is modularity. This modularity opens the way to various future upgrades: use-cases enabled by additional modules

(Section V-A), as well as possible upgrades to the core modules (Section V-B).

A. APPLICATION USE CASES

- Inline imaging cytometry: The addition of a high-speed camera/detection module (and ideally a cell incubation module) could enable inline imaging cytometry.
- Cell sorting: The addition of a droplet sorting module, together with the aforementioned imaging cytometry modules, could enable droplet-based cell sorting for further downstream processing of select cells or cell lines. The single-cell resolution and chemical isolation provided by droplets could greatly increase the throughput, while reducing reagent and sample waste compared to current state-of-the-art flow cytometry setups.

B. POSSIBLE UPGRADES TO THE PROTOTYPE SYSTEM

- To improve the droplet capture rate and reliability, an additional ESP32, or a similar low-cost device with an SPI bus and two cores, could be placed between the RPI and ADC to take over task 3 from the RPI. Additionally, the added computational power could enable more complex waveform analysis (e.g., waveform slope measurement and droplet lensing effect detection).
- To improve the droplet size and generation frequency control accuracy and fault tolerance, machine learning models could be implemented on the RPI.
- To improve automation, the following features could contribute: self-priming, self-cleaning, auto-chip-positioner, auto-pinhole-positioner, self-analyzing (e.g., detection of blockages or leaks in the fluidics module), auto-focusing, and auto-calibration-ranging.
- To improve the user interface, the GUI, after calibration, could offer feasible droplet size and generation frequency ranges, with highlighted combinations yielding the best CV% for that specific chip and position. Furthermore, by user request, the GUI could poll captured waveform samples during operation.
- To correlate relatively inexpensively and rapidly measured droplet sizes from their shadows to real droplet volume, a secondary in-line camera setup could be joined in the communication line over eCAL. To image droplets, as proposed in Section V-A, during cytometry.

VI. CONCLUSION

A proof-of-concept prototype of an integrated, modular system for automated aqueous droplet generation with high monodispersity was presented. The system measured droplet sizes and generation rates using a visible spectrum LED-photodiode setup aligned with the cross-junction of the FFD, converting the droplet's shadow to voltage. Resulting peak-to-peak voltages were correlated with relative size of the droplet whereas the time between the beginnings of droplets were used to obtain the generation rate. We reported on the assembly and the underlying working principle, as well as the experimental evaluation of the performance of the prototype, both on a module level and system level. Module-level evaluation and comparison to reference syringe pumps indicated a 12 times reduction in pressure stabilization times. The system-level evaluation proved that the system was capable of repeatedly generating droplets with stability comparable to other state-of-the-art droplet generation systems. Droplet generation stability was proven over 2 different carrier media and 3 different junction geometries in total. The lowest relative droplet size CV% recorded was 1.77% ($\sim$0.00031 PDI) using Chip B with fluid phase combination B. With droplets controllably generated in tested relative size targets between 2.0 to 4.4 V, polydisperse (PDI $>$ 0.1) droplets with a stable size distribution can also be generated. Unique characteristics from relationships between droplet size/generation rate and chip geometry were made observable through automated calibration and parameter target test series with different chips. Conditional droplet generation rate analysis also revealed high linear correlation regions for the ''SD of the generation rate'' with the ''target rate'' for chips B and C, from 200 Hz up to 600 Hz and 500 Hz respectively. In conclusion, the presented prototype system has comparable droplet generation performance metrics to other state-of-the-art droplet generation setups, but offers several advantages: 1) modularity, integration, wireless communication and the option to run from battery power, enabling portability; 2) affordability; 3) automation and ease of use, increasing repeatability of results and allowing transfer of protocols between labs, as well as reducing manual workloads; 4) user-friendly (re-)calibration of chip alignment.

ACKNOWLEDGMENT

The authors would like to thank researcher Simona Bartkova (Department of Chemistry and Biotechnology) from the Tallinn University of Technology with their assistance with droplet imaging and droplet generation chip fabrication methods and tools. The perfluoropolyether (PFPE)-poly(ethylene glycol) (PEG)-PFPE triblock surfactant, used with fluorinated oil, was a kind gift from Prof. Piotr Garstecki from the Institute of Physical Chemistry, Polish Academy of Sciences.

REFERENCES

[1] T. S. Kaminski, O. Scheler, and P. Garstecki, ''Droplet microfluidics for microbiology: Techniques, applications and challenges,'' *Lab Chip*, vol. 16, no. 12, pp. 2168–2187, 2016, doi: 10.1039/C6LC00367B.

[2] W. Postek, P. Gargulinski, O. Scheler, T. S. Kaminski, and P. Garstecki, ''Microfluidic screening of antibiotic susceptibility at a single-cell level shows the inoculum effect of cefotaxime on E. coli,'' *Lab Chip*, vol. 18, no. 23, pp. 3668–3677, 2018, doi: 10.1039/C8LC00916C.

[3] O. Scheler, K. Makuch, P. R. Debski, M. Horka, A. Ruszczak, N. Pacocha, K. Sozański, O.-P. Smolander, W. Postek, and P. Garstecki, ''Droplet-based digital antibiotic susceptibility screen reveals single-cell clonal heteroresistance in an isogenic bacterial population,'' *Sci. Rep.*, vol. 10, no. 1, p. 3282, Feb. 2020, doi: 10.1038/s41598-020-60381-z.

[4] K. Pärnamets, T. Pardy, A. Koel, T. Rang, O. Scheler, Y. Le Moullec, and F. Afrin, ''Optical detection methods for high-throughput fluorescent droplet microflow cytometry,'' *Micromachines*, vol. 12, no. 3, p. 345, Mar. 2021, doi: 10.3390/mi12030345.

[5] M. Li, H. Liu, S. Zhuang, and K. Goda, ''Droplet flow cytometry for single-cell analysis,'' *RSC Adv.*, vol. 11, no. 34, pp. 20944–20960, Jun. 2021, doi: 10.1039/D1RA02636D.

[6] Y. Ding, P. D. Howes, and A. J. Demello, "Recent advances in droplet microfluidics," *Anal. Chem.*, vol. 92, no. 1, pp. 132–149, Jan. 2020, doi: 10.1021/acs.analchem.9b05047.

[7] S. Stavrakis, G. Holzner, J. Choo, and A. de Mello, "High-throughput microfluidic imaging flow cytometry," *Current Opinion Biotechnol.*, vol. 55, pp. 36–43, Feb. 2019, doi: 10.1016/j.copbio.2018.08.002.

[8] C. Cha, J. Oh, K. Kim, Y. Qiu, M. Joh, S. R. Shin, X. Wang, G. Camci-Unal, K.-T. Wan, R. Liao, and A. Khademhosseini, "Microfluidics-assisted fabrication of gelatin-silica core–shell microgels for injectable tissue constructs," *Biomacromolecules*, vol. 15, no. 1, pp. 283–290, Jan. 2014, doi: 10.1021/BM401533Y.

[9] R. Samanipour, Z. Wang, A. Ahmadi, and K. Kim, "Experimental and computational study of microfluidic flow-focusing generation of gelatin methacrylate hydrogel droplets," *J. Appl. Polym. Sci.*, vol. 133, no. 29, pp. 1-10, Aug. 2016, doi: 10.1002/APP.43701.

[10] W. Zeng, H. Fu, and S. Li, "Characterization of the pressure-driven flows for droplet microfluidics," in *Proc. CSAA/IET Int. Conf. Aircr. Utility Syst. (AUS)*, Jun. 2018, pp. 309–313, doi: 10.1049/cp.2018.0090.

[11] W. Zeng, S. Yang, Y. Liu, T. Yang, Z. Tong, X. Shan, and H. Fu, "Precise monodisperse droplet generation by pressure-driven microfluidic flows," *Chem. Eng. Sci.*, vol. 248, Feb. 2022, Art. no. 117206, doi: 10.1016/J.CES.2021.117206.

[12] X. Duan, Z. Zheng, Y. Luo, and C. Song, "Closed-loop feedback control for droplet-based microfluidics: A characteristic investigation on passive and on-demand droplet generation," *Proc. SPIE*, vol. 12550, pp. 183–188, Jan. 2023, doi: 10.1117/12.2666602.

[13] W. Zeng and H. Fu, "Precise monodisperse droplet production in a flow-focusing microdroplet generator," *Chem. Eng. Res. Des.*, vol. 160, pp. 321–325, Aug. 2020, doi: 10.1016/J.CHERD.2020.06.002.

[14] N. Wang, R. Liu, N. Asmare, C.-H. Chu, O. Civelekoglu, and A. F. Sarioglu, "Closed-loop feedback control of microfluidic cell manipulation via deep-learning integrated sensor networks," *Lab Chip*, vol. 21, no. 10, pp. 1916–1928, 2021, doi: 10.1039/d1lc00076d.

[15] E.-C. Yeh, C.-C. Fu, L. Hu, R. Thakur, J. Feng, and L. P. Lee, "Self-powered integrated microfluidic point-of-care low-cost enabling (SIMPLE) chip," *Sci. Adv.*, vol. 3, no. 3, Mar. 2017, Art. no. e1501645, doi: 10.1126/sciadv.1501645.

[16] D. F. Crawford, C. A. Smith, and G. Whyte, "Image-based closed-loop feedback for highly mono-dispersed microdroplet production," *Sci. Rep.*, vol. 7, no. 1, pp. 1–9, Sep. 2017, doi: 10.1038/s41598-017-11254-5.

[17] B. Miller, "Manipulation of microfluidic droplets," U.S. Patent EP2 411 148 B1, Mar. 23, 2010.

[18] B. van Elburg, G. Collado-Lara, G.-W. Bruggert, T. Segers, M. Versluis, and G. Lajoinie, "Feedback-controlled microbubble generator producing one million monodisperse bubbles per second," *Rev. Sci. Instrum.*, vol. 92, no. 3, Mar. 2021, Art. no. 035110, doi: 10.1063/5.0032140.

[19] N. Gyimah, O. Scheler, T. Rang, and T. Pardy, "Can 3D printing bring droplet microfluidics to every lab?—A systematic review," *Micromachines*, vol. 12, no. 3, p. 339, Mar. 2021, doi: 10.3390/mi12030339.

[20] TalTech-LoC. *HW-Open-Fluidic-Infra*. Accessed: May 16, 2023. [Online]. Available: https://github.com/taltechloc/hw-open-fluidic-infra

[21] N. Gyimah, O. Scheler, T. Rang, and T. Pardy, "Digital twin for controlled generation of water-in-oil microdroplets with required size," in *Proc. 23rd Int. Conf. Thermal, Mech. Multi-Phys. Simul. Experiments Microelectron. Microsystems (EuroSimE)*, Apr. 2022, pp. 1–7, doi: 10.1109/EuroSimE54907.2022.9758876.

[22] N. Gyimah, R. Joemaa, K. Parnamets, O. Scheler, T. Rang, and T. Pardy, "PID controller tuning optimization using genetic algorithm for droplet size control in microfluidics," in *Proc. 18th Biennial Baltic Electron. Conf. (BEC)*, Oct. 2022, pp. 1–6, doi: 10.1109/BEC56180.2022.9935596.

[23] R. Joemaa, M. Grosberg, T. Rang, and T. Pardy, "Low-cost, portable dual-channel pressure pump for droplet microfluidics," in *Proc. 45th Jubilee Int. Conv. Inf., Commun. Electron. Technol. (MIPRO)*, May 2022, pp. 205–211, doi: 10.23919/MIPRO55190.2022.9803371.

[24] M. Grosberg, R. Jõemaa, P. Tamas, and T. Rang. (2022). *Wireless Microfluidic Dual-Channel Pressure Pump*. [Online]. Available: https://www.etis.ee/Portal/IndustrialProperties/Display/353426b9-f02b-44b2-b581-e8f21363157a

[25] K. Ashraf, Y. L. Moullec, T. Pardy, and T. Rang, "Model-based system architecture for event-triggered wireless control of bio-analytical devices," in *Proc. 24th Euromicro Conf. Digit. Syst. Design (DSD)*, Sep. 2021, pp. 465–471, doi: 10.1109/DSD53832.2021.00076.

[26] Alphabet. (2022). *Protocol Buffers | Google Developers*. Accessed: Oct. 31, 2022. [Online]. Available: https://developers.google.com/protocol-buffers/docs/reference/overview

[27] Eclipse. (2022). *Welcome to Eclipse eCALTM—Eclipse eCALTM Documentation*. Accessed: Oct. 31, 2022. [Online]. Available: https://eclipse-ecal.github.io/ecal/

[28] K. Parnamets, A. Koel, T. Pardy, and T. Rang, "Open source hardware cost-effective imaging sensors for high-throughput droplet microfluidic systems," in *Proc. 26th Int. Conf. Electron.*, Jun. 2022, pp. 1–6, doi: 10.1109/IEEECONF55059.2022.9810383.

[29] N. A. Prabatama, R. Joemaa, K. Hegedus, and T. Pardy, "Low-cost open-source flow velocity sensor for droplet generators," in *Proc. 18th Biennial Baltic Electron. Conf. (BEC)*, Oct. 2022, pp. 1–4, doi: 10.1109/BEC56180.2022.9935606.

[30] J. Caldwell. (2014). *An IMPORTANT NOTICE at the End of This TI Reference Design Addresses Authorized Use, Intellectual Property Matters and Other Important Disclaimers and Information*. Accessed: May 12, 2023. [Online]. Available: www.ti.com

[31] O. Scheler, T. S. Kaminski, A. Ruszczak, and P. Garstecki, "Dodecylresorufin (C12R) outperforms resorufin in microdroplet bacterial assays," *ACS Appl. Mater. Interfaces*, vol. 8, no. 18, pp. 11318–11325, May 2016, doi: 10.1021/acsami.6b02360.

[32] TalTech-LoC. (2020). *HW-MVP-Chip*. Accessed: Sep. 21, 2022. [Online]. Available: https://github.com/taltechloc/hw-mvp-chip

[33] (2022). *BioMEMS Group*. Accessed: Oct. 31, 2022. [Online]. Available: https://biomems.hu/

[34] W. Zeng, S. Li, and Z. Wang, "Closed-loop feedback control of droplet formation in a T-junction microdroplet generator," *Sens. Actuators A, Phys.*, vol. 233, pp. 542–547, Sep. 2015, doi: 10.1016/j.sna.2015.08.002.

[35] Y. Xie, A. J. Dixon, J. M. R. Rickel, A. L. Klibanov, and J. A. Hossack, "Closed-loop feedback control of microbubble diameter from a flow-focusing microfluidic device," *Biomicrofluidics*, vol. 14, no. 3, May 2020, Art. no. 034101, doi: 10.1063/5.0005205.

[36] S. Motaghi, M. Nazari, N. Sepehri, and A. Mahdavi, "Control of droplet size in a two-phase microchannel using PID controller: A novel experimental study," *Amirkabir J. Mech. Eng. Amirkabir J. Mech. Eng*, vol. 53, no. 7, pp. 1013–1016, 2021, doi: 10.22060/mej.2020.18250.6783.

[37] H. Fu, W. Zeng, S. Li, and S. Yuan, "Electrical-detection droplet microfluidic closed-loop control system for precise droplet production," *Sens. Actuators A, Phys.*, vol. 267, pp. 142–149, Nov. 2017, doi: 10.1016/j.sna.2017.09.043.

RAUNO JÕEMAA was born in Estonia, in 1991. He received the bachelor's degree in electronics and bionics and the master's degree in communicative electronics from the Tallinn University of Technology, where he is currently pursuing the Ph.D. degree with the Thomas Johann Seebeck Department of Electronics. He is a Junior Researcher with the Department of Chemistry and Biotechnologies, Tallinn University of Technology. His current research interests include electronics and microfluidics.

NAFISAT GYIMAH received the B.S. degree in electrical and electronic engineering from the Kwame Nkrumah University of Technology, Kumasi, Ghana, in 2013, and the M.S. degree in communicative electronics from the Tallinn University of Technology, Tallinn, Estonia, in 2020, where she is currently pursuing the Ph.D. degree in high-speed droplet microfluidics sorting and encapsulation. From November 2021 to January 2022, she was with SelfDiagnostics Deutschland GmbH, where she focused on the thermal and electrical characterization of SARS-CoV2 microfluidic multitest kits. She was a Cognitronics Engineer with the Tallinn University of Technology, from June 2020 to December 2020. Her current research interests include lab-on-a-chip, droplet microfluidic system control, and flow control simulations using computational fluid dynamics (CFD).

KANWAL ASHRAF received the bachelor's degree in electrical engineering from the University of the Punjab, Pakistan, and the joint-international master's degree in smart system integration from Heriot-Watt University, U.K., the University of South-Eastern Norway (USN), Norway, and the Budapest University of Technology and Economics (BME), Hungary, in 2020. She is currently pursuing the Ph.D. degree with the Tallinn University of Technology, Estonia. Her current research interests include the application of wireless communication in CPSs and the co-design of wireless networked control systems for bioanalytical applications.

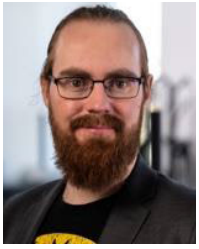

KAISER PÄRNAMETS (Member, IEEE) was born in Tallinn, Estonia, in January 1989. He received the B.Sc. and M.Sc. degrees in engineering from the Tallinn University of Technology, in 2013 and 2016, respectively, where he is currently pursuing the Ph.D. degree. From 2014 to 2017, he was a hardware engineer in the electronics industry and has been an electronics lecturer for bachelor's and master's students, since 2018. His current research interests include lab-on-a-chip and microfluidics.

ALEXANDER ZAFT was born in 1997. He received the bachelor's and master's degrees in computer science from the University of Würzburg, Germany, in 2019 and 2022, respectively. In Summer 2022, he joined the Lab-on-a-Chip Group, Tallinn University of Technology, as an Intern. Since November 2022, he has been a Software Engineer with Heinz-Maier-Leibnitz Zentrum, Garching, Germany.

OTT SCHELER received the Ph.D. degree in biotechnology from the University of Tartu, Estonia, in 2012. He was a Postdoctoral Researcher of microfluidics with the Institute of Physical Chemistry, Polish Academy of Sciences, from 2014 to 2018. After that, he joined the Tallinn University of Technology, where he is currently an Associate Professor of microfluidics with the Department of Chemistry and Biotechnology. His current research interests include microfluidics, microbiology, and biotechnology.

TOOMAS RANG (Senior Member, IEEE) received the Ph.D. degree in semiconductor electronics from the Hungarian Academy of Sciences, in 1981. He is currently a Professor Emeritus with the Thomas Johann Seebeck Department of Electronics and a Senior Research Fellow with the Department of Chemistry and Biotechnologies, Tallinn University of Technology, Estonia. He has supervised 15 Ph.D. students and has fulfilled the PI position in several European and domestic research and industrial projects. His current research interest includes applied microfluidics approaches for lab-on-chip applications. He is the Initiator and today the honor Chairperson of the Baltic Electronics Conference (BEC) Series, in 1987, supported by IEEE, since 1996.

TAMÁS PARDY (Member, IEEE) received the M.Sc. degree in info-bionics engineering from Peter Pazmany Catholic University, Budapest, Hungary, in 2014, and the Ph.D. degree in electronics and telecommunication from the Tallinn University of Technology, Tallinn, Estonia, in 2018. He is currently a Senior Researcher with the Tallinn University of Technology. He has supervised one Ph.D. thesis and five M.Sc. thesis and has authored or coauthored over 20 scientific publications. His current research interest includes flow- and temperature control of lab-on-a-chip devices.